Journal of
Mechanics of
Materials and Structures

A SIMPLE SCALAR DIRECTIONAL HARDENING MODEL FOR THE BAUSCHINGER EFFECT COMPARED WITH A TENSORIAL MODEL

Martin Kroon and M. B. Rubin

Volume 15, No. 4 July 2020

msp

JOURNAL OF MECHANICS OF MATERIALS AND STRUCTURES
Vol. 15, No. 4, 2020
https://doi.org/10.2140/jomms.2020.15.511

A SIMPLE SCALAR DIRECTIONAL HARDENING MODEL FOR THE BAUSCHINGER EFFECT COMPARED WITH A TENSORIAL MODEL

MARTIN KROON AND M. B. RUBIN

Modeling the Bauschinger effect is usually accomplished by introducing a second-order back-stress or directional hardening tensor. The objective of this paper is to propose a simpler scalar model of the Bauschinger effect based on a scalar directional hardening parameter that is determined by integration of an evolution equation. The behavior of this scalar model is compared to a tensorial model for a number of load cases. Strongly objective numerical algorithms are developed for integrating the evolution equations for both the tensorial and scalar models. Also, a consistent tangent is developed for both models. Obviously, the numerical implementation of the scalar model is significantly less complicated than for the tensorial model. Examples show that the tensorial and scalar models predict the same results for cyclic proportional triaxial extension and triaxial compression loadings. In contrast, the tensorial model predicts a Bauschinger effect for cyclic proportional pure torsion loading which is not predicted by the scalar model. More complicated examples with nonproportional loading paths and inhomogeneous deformations indicate that, relative to the tensorial model, the scalar model accounts for directional hardening fairly well and the simplicity of the model makes it an attractive option to add to isotropic hardening models.

1. Introduction

The inelastic response of isotropic metals typically exhibits some form of hardening. The simplest model for hardening introduces an isotropic hardening variable κ, which is determined by integrating an evolution equation for its rate. Cyclic loading in uniaxial stress using a model with only isotropic hardening indicates that the magnitude of stress in tension at the onset of unloading is the same as that in compression at the onset of inelastic response during reverse loading. For many metals, however, cyclic loading in uniaxial stress also exhibits a Bauschinger effect [Bauschinger 1881], which is observed as a reduced magnitude of stress and a rounding of the stress-strain curve at the onset of reverse loading. A review of aspects of the Bauschinger effect in metals up until 1979 can be found in [Sowerby et al. 1979]. There the physical reason for the Bauschinger effect is described as long range stresses caused by inhomogeneous deformations of the grains that introduce directionality of the resistance to inelastic flow.

The introduction in [Langer et al. 2010] reviews comments by major researchers of hardening in metals who conclude that phenomenological models of hardening are necessary since a theory of hardening based on first-principles has not been developed. Langer et al. [2010] then proceed to develop a theory that characterizes the thermodynamically irreversible nature of dislocations which successfully predicts the strain hardening of copper over a wide range of temperatures and strain rates. Specifically, they introduce an effective temperature of dislocations and a second-law for externally driven systems within the context

Keywords: Bauschinger effect, finite deformation, isotropic elastic-inelastic response, numerical algorithm, scalar directional hardening.

of homogeneous deformations. However, this theory is not relevant for quasistatic experiments. A recent thermodynamical theory based on nonuniform plastic deformations, which account for excess dislocations due to the incompatibility of plastic distortion, has been developed in [Le and Tran 2018]. This theory explains that the Bauschinger effect is due to movement and annihilation of excess dislocations during load reversal but it does not predict the observed smoothing of the stress-strain curve during load reversal.

Within the context of small deformations, [Prager 1949] used a yield function with the stress replaced by the difference between the stress and a kinematic hardening parameter (sometimes referred to as a back-stress) which he attributed to a conference abstract by Reuss [1935]. This model captures the Bauschinger effect but it exhibits a sharp elastic-inelastic transition. An early model for cyclic loading that captures the Bauschinger effect and smooths the elastic-inelastic transition with a finite number of segments was introduced by Besseling [1958], who used a number of inelastic elements that are activated at different stress levels. More modern phenomenological continuum models typically introduce kinematic hardening, with the yield surface being expressed as a function of the stress $\boldsymbol{T}$ minus back-stress tensor $\boldsymbol{\beta}$. The original report by [Armstrong and Frederick 1966] has been republished with a historical introduction. Another feature of this formulation of kinematic hardening is that the inelastic deformation rate is proportional to the difference between the stress and the kinematic hardening variable. This allows the model to capture more complicated response for nonproportional loadings. A review of plastic and viscoplastic response with kinematic hardening can be found in [Chaboche 2008].

Directional hardening is an alternative to kinematic hardening (e.g., [Bodner 1968]). In this model an effective yield strength is determined by a function of the isotropic hardening variable and the inner product of the stress with a symmetric directional hardening tensor $\boldsymbol{\beta}$ to account for different yielding properties in different directions. Moreover, the inelastic deformation rate remains proportional to the deviatoric stress. Within the context of the directional hardening formulation, the direction of the inelastic deformation rate was modified in [Rubin and Bodner 1995] to include a component normal to the deviatoric stress which produced a reduced modulus for nonproportional loading. For both of these directional hardening models the rate of material dissipation remains nonnegative. In contrast, depending on the formulation of kinematic hardening, the model can produce negative material dissipation for proportional cyclic uniaxial stress loading if inelasticity occurs during unloading before the stress changes sign as the material goes into reverse loading. A more recent alternative formulation to kinematic hardening, which models the Bauschinger effect, can be found in [Barlat et al. 2011].

For large deformations with the back-stress tensor $\boldsymbol{\beta}$ being subtracted from the Cauchy stress $\boldsymbol{T}$ in the yield function it is necessary to propose an evolution equation for $\boldsymbol{\beta}$ which ensures that $\boldsymbol{\beta}$ rotates like $\boldsymbol{T}$ under Superposed Rigid Body Motions (SRBM). This means that the modeling includes an inelastic spin tensor that needs a constitutive equation (e.g., [Bammann 1990]).

To model more complicated multiaxial response, [Armstrong and Frederick 1966] introduced an effective kinematic hardening tensor as the sum of a number of hardening tensors which each were determined by evolution equations. Similarly, motivated by the work in [Hollenstein et al. 2013], which proposed a large deformation model with a smooth elastic-inelastic transition for both rate independent and rate-dependent response, LS-DYNA [Gladman 2018] developed a generalized model (MAT_275) which includes a number of elastic distortional deformation tensors to model more complicated inelastic effects for cyclic and multiaxial loadings with relaxation.

The objective of this paper is to propose a simplified scalar model for the Bauschinger effect which introduces a scalar evolution equation for a directional hardening parameter β. The responses of this scalar model are compared with those of a tensorial model which introduces an evolution equation for a directional hardening tensor $\boldsymbol{\beta}$. The simplified scalar model predicts the same results as the tensorial model for cyclic proportional triaxial extension and triaxial compression loadings. However, in contrast with the tensorial model, the scalar model cannot predict the Bauschinger effect for cyclic proportional pure torsion loading. Robust and strongly objective numerical integration algorithms are developed for both the scalar model and tensorial models. In this regard, it is recalled [Rubin and Papes 2011] that an algorithm will be strongly objective if all of the numerical estimates of tensorial quantities satisfy the same transformation relations under SRBM as the exact tensorial measures. Moreover, it is shown that the scalar model predicts nearly the same effective yield strength contours as the tensorial model for example problems with nonproportional loading and inhomogeneous deformation.

An outline of this paper is as follows: Section 2 provides an outline of the general theoretical framework to be used, whereas Section 3 describes the details of the different hardening models employed. Section 4 summarizes the objectivity properties of relevant entities in the theoretical framework, and Section 5 contains a description of a strongly objective numerical integration procedure for the state variables, including an algorithmic tangent stiffness. A number of numerical examples are provided in Section 6, and a discussion and some concluding remarks are given in Section 7.

2. Basic equations

Let $\boldsymbol{x}$ and $\boldsymbol{v} = \dot{\boldsymbol{x}}$ denote the position and velocity, respectively, of a material point in the current configuration at time t, where $\dot{(\,)}$ denotes the material time derivative. Then, the velocity gradient is given by $\boldsymbol{L} = \partial\boldsymbol{v}/\partial\boldsymbol{x}$, and the rate of deformation $\boldsymbol{D}$ and the spin $\boldsymbol{W}$ are defined by

$$\boldsymbol{L} = \boldsymbol{D} + \boldsymbol{W}, \qquad \boldsymbol{D} = \tfrac{1}{2}(\boldsymbol{L} + \boldsymbol{L}^T), \quad \boldsymbol{W} = \tfrac{1}{2}(\boldsymbol{L} - \boldsymbol{L}^T). \tag{1}$$

The need for an Eulerian formulation of evolution equations for finite deformation elastic-inelastic response has been discussed in a series of papers (e.g., [Rubin and Attia 1996; Rubin 2012]). This Eulerian formulation is insensitive to the choice of reference configuration, an intermediate configuration, a total deformation measure and an inelastic deformation measure. Eckart [1948] seems to be the first to propose an evolution equation directly for elastic deformation that is used to determine stress for finite elastic-inelastic deformations of solids. Leonov [1976] proposed similar equations for polymeric liquids.

Within the context of the Eulerian formulation of isotropic, hyperelastic-inelastic materials, Rubin and Attia [1996] proposed evolution equations for an elastic dilatational deformation J_e and a symmetric, positive-definite, unimodular second order elastic distortional deformation tensor $\bar{\boldsymbol{B}}_\mathrm{e}$. In the absence of inelastic dilatational deformation, the elastic dilatation is defined by

$$J_\mathrm{e} = \rho_\mathrm{z}/\rho \tag{2}$$

with ρ being the current mass density and ρ_z being its zero-stress value. Furthermore, the evolution equations for these quantities were proposed in the forms

$$\frac{\dot{J}_\mathrm{e}}{J_\mathrm{e}} = \boldsymbol{D} : \boldsymbol{I}, \quad \dot{\bar{\boldsymbol{B}}}_\mathrm{e} = \boldsymbol{L}\bar{\boldsymbol{B}}_\mathrm{e} + \bar{\boldsymbol{B}}_\mathrm{e}\boldsymbol{L}^T - \tfrac{2}{3}(\boldsymbol{D} : \boldsymbol{I})\bar{\boldsymbol{B}}_\mathrm{e} - \Gamma\boldsymbol{A}_\mathrm{p}, \quad \boldsymbol{A}_\mathrm{p} = \bar{\boldsymbol{B}}_\mathrm{e} - \left(\frac{3}{\bar{\boldsymbol{B}}_\mathrm{e}^{-1} : \boldsymbol{I}}\right)\boldsymbol{I}, \tag{3}$$

where the scalar function $\Gamma \geq 0$ controls the magnitude of inelastic distortional deformation rate, and the tensor $\boldsymbol{A}_{\mathrm{p}}$ controls the direction of inelastic distortional deformation rate. This form ensures that inelastic deformation rate causes a tendency for $\bar{\boldsymbol{B}}_{\mathrm{e}}$ to approach the identity $\boldsymbol{I}$ and for $\bar{\boldsymbol{B}}_{\mathrm{e}}$ to remain a unimodular tensor. The evolution equation for J_{e} is appropriate for nonporous metals with no inelastic dilatation rate and can be determined by the conservation of mass equation. Also, $\boldsymbol{A} : \boldsymbol{B} = \mathrm{tr}(\boldsymbol{A}\boldsymbol{B}^T)$ denotes the inner product of two second order tensors $\boldsymbol{A}$ and $\boldsymbol{B}$ and $\boldsymbol{I}$ is the second order unit tensor.

The formulation in [Rubin and Cardiff 2017] simplifies that in [Simo 1992, 2.19a] and [Simo 1998, §50] and recorded in [Simo and Hughes 1998, Box 9.1], which corrected that proposed in [Simo 1988, Table 1]. Specifically, for a neo-Hookean material, the strain energy function Σ per unit mass can be specified in the form

$$\rho_{\mathrm{z}}\Sigma = \tfrac{1}{2}K(J_{\mathrm{e}} - 1)^2 + \tfrac{1}{2}\mu(\alpha_1 - 3), \tag{4}$$

where K and μ are the zero-stress bulk and shear modulus, respectively, and the first invariant α_1 of the elastic distortional deformation tensor $\bar{\boldsymbol{B}}_{\mathrm{e}}$ satisfies the equations

$$\alpha_1 = \bar{\boldsymbol{B}}_{\mathrm{e}} : \boldsymbol{I} \geq 3, \qquad \dot{\alpha}_1 = 2\bar{\boldsymbol{B}}'_{\mathrm{e}} : \boldsymbol{D} - \Gamma \boldsymbol{A}_p : \boldsymbol{I}, \tag{5}$$

where a superscript prime $(\bullet)'$ is added to the symbol of a tensor to denote its deviatoric part. For example, the deviatoric part $\bar{\boldsymbol{B}}'_{\mathrm{e}}$ of $\bar{\boldsymbol{B}}_{\mathrm{e}}$ is defined by

$$\bar{\boldsymbol{B}}'_{\mathrm{e}} = \bar{\boldsymbol{B}}_{\mathrm{e}} - \tfrac{1}{3}(\bar{\boldsymbol{B}}_{\mathrm{e}} : \boldsymbol{I})\boldsymbol{I}. \tag{6}$$

It follows that the Cauchy stress $\boldsymbol{T}$ associated with this strain energy function is given by

$$\boldsymbol{T} = -p\boldsymbol{I} + \boldsymbol{T}', \quad p = -\rho_{\mathrm{z}}\frac{\partial \Sigma}{\partial J_{\mathrm{e}}} = K(1 - J_{\mathrm{e}}), \quad \boldsymbol{T}' = 2J_{\mathrm{e}}^{-1}\rho_{\mathrm{z}}\frac{\partial \Sigma}{\partial \alpha_1}\bar{\boldsymbol{B}}'_{\mathrm{e}} = J_{\mathrm{e}}^{-1}\mu\bar{\boldsymbol{B}}'_{\mathrm{e}}. \tag{7}$$

Also, the rate of material dissipation $\mathcal{D}$ automatically satisfies the restriction that

$$\mathcal{D} = \boldsymbol{T} : \boldsymbol{D} - \rho\dot{\Sigma} = \tfrac{1}{2}J_{\mathrm{e}}^{-1}\mu\Gamma\boldsymbol{A}_{\mathrm{p}} : \boldsymbol{I} \geq 0. \tag{8}$$

Next, consider a yield function of the form

$$g = 1 - \frac{H\kappa}{\gamma_e}, \tag{9}$$

with $g < 0$ implying elastic response, and $g = 0$ defining the elastic-inelastic boundary. In this yield function, the effective elastic distortional strain γ_e is defined by

$$\gamma_e = \tfrac{1}{2}\sqrt{\tfrac{3}{2}\bar{\boldsymbol{B}}'_{\mathrm{e}} : \bar{\boldsymbol{B}}'_{\mathrm{e}}}. \tag{10}$$

In the expression (9) for the yield function g, κ is a positive measure of isotropic hardening that is determined by integrating an evolution equation (16) defined later and H is a scalar measure of directional hardening defined later in (19) for the tensorial model or in (25) for the scalar model.

A simple rate-independent version of the smooth elastic-inelastic transition model proposed in [Hollenstein et al. 2013] is obtained by using the yield function g in (9) and specifying the function Γ in the form

$$\Gamma = b_1\dot{\varepsilon}\langle g\rangle, \quad b_1 > 0, \tag{11}$$

where b_1 is a constant that controls the smoothness of the elastic-inelastic transition, the effective total distortional rate of deformation $\dot{\varepsilon}$ is defined by

$$\dot{\varepsilon} = \sqrt{\tfrac{2}{3}\boldsymbol{D}' : \boldsymbol{D}'}, \tag{12}$$

with the Macaulay brackets $\langle g \rangle$ defined by

$$\langle g \rangle = \max(g, 0). \tag{13}$$

From (3) and (11) it is observed that the material response is elastic when the inelastic deformation rate vanishes ($g \leq 0$) and is inelastic with an overstress when $g > 0$. Moreover, this model does not require loading and unloading conditions. Large values of b_1 reduce the magnitude of the overstress with the response asymptotically approaching that predicted by standard loading and unloading conditions with no overstress ($g \leq 0$) in the limit that $b_1 \to \infty$.

Even though a measure of plastic deformation is not necessary in the present Eulerian formulation, an equivalent plastic deformation may still be introduced to identify regions in a structure which have experienced inelastic deformation. It can be shown that for small deformations, the inelastic distortional deformation rate can be approximated by

$$\dot{\boldsymbol{\varepsilon}}_\mathrm{p} \approx \tfrac{1}{2}\Gamma \bar{\boldsymbol{B}}'_\mathrm{e}. \tag{14}$$

Then, the equivalent inelastic deformation rate is defined as

$$\dot{\varepsilon}_\mathrm{p} = \sqrt{\tfrac{2}{3}\dot{\boldsymbol{\varepsilon}}_\mathrm{p} : \dot{\boldsymbol{\varepsilon}}_\mathrm{p}} = \tfrac{1}{2}\Gamma\sqrt{\tfrac{2}{3}\bar{\boldsymbol{B}}'_\mathrm{e} : \bar{\boldsymbol{B}}'_\mathrm{e}} = \tfrac{2}{3}\Gamma\gamma_\mathrm{e}. \tag{15}$$

3. Models for hardening

3.1. ***Prerequisites.*** A combination of isotropic and directional hardening is used. The same model for isotropic hardening is used throughout this work, whereas two formulations of directional hardening models are explored:

(a) a formulation using a second-order directional hardening tensor $\boldsymbol{\beta}$, and

(b) a formulation using a single scalar state variable β.

3.2. ***Isotropic hardening.*** For all models discussed in this paper, the isotropic hardening variable κ is determined by the evolution equation [Chan et al. 1988]

$$\dot{\kappa} = m_1\Gamma(\kappa_\mathrm{s} - \kappa) - m_2(\kappa - \kappa_\mathrm{a}), \quad \Gamma \geq 0, \quad m_1 \geq 0, \quad m_2 \geq 0, \quad \kappa_\mathrm{a} \leq \kappa \leq \kappa_\mathrm{s} > 0. \tag{16}$$

This evolution equation includes a competition of strain hardening rate and thermal recovery rate. Strain hardening causes a tendency for κ to approach its saturated value κ_s with its rate controlled by the constant m_1. Thermal recovery causes a tendency for κ to approach its fully annealed value κ_a with its rate controlled by the constant m_2.

3.3. ***A tensor-based model for directional hardening.*** A formulation of directional hardening, using a second-order tensor, is now presented. To distinguish between the different models for directional hardening, the present model is termed “Model T” (“T” for “tensor”). Motivated by the work in [Chan et al. 1988], the evolution equation for the directional hardening tensor $\boldsymbol{\beta}$ is proposed in the form

$$\hat{\boldsymbol{\beta}} = m_3\Gamma(\beta_s\boldsymbol{U} - \boldsymbol{\beta}) - m_4\boldsymbol{\beta}, \quad 0 \le \beta_s < 1, \quad m_3 \ge 0, \quad m_4 \ge 0, \tag{17}$$

where $\hat{\boldsymbol{\beta}}$ denotes the objective Jaumann derivative and is defined by

$$\hat{\boldsymbol{\beta}} \equiv \dot{\boldsymbol{\beta}} - (\boldsymbol{W}\boldsymbol{\beta} + \boldsymbol{\beta}\boldsymbol{W}^T). \tag{18}$$

The function H, which accounts for directional hardening in the yield function (9), is specified by

$$H = H_T = 1 + \boldsymbol{\beta} : \boldsymbol{U}. \tag{19}$$

In these equations, $\boldsymbol{\beta}$ is a symmetric, deviatoric, directional hardening tensor, $\boldsymbol{U}$ is defined by the direction of the deviatoric elastic distortional deformation tensor $\bar{\boldsymbol{B}}'_e$, such that

$$\boldsymbol{\beta}^T = \boldsymbol{\beta}, \quad \boldsymbol{\beta} : \boldsymbol{I} = 0, \quad \boldsymbol{U} = \frac{\bar{\boldsymbol{B}}'_e}{|\bar{\boldsymbol{B}}'_e|}, \quad \boldsymbol{U}^T = \boldsymbol{U}, \quad \boldsymbol{U} : \boldsymbol{I} = 0, \quad \boldsymbol{U} : \boldsymbol{U} = 1. \tag{20}$$

Hence, the value of H_T in (19) depends on the magnitude of $\boldsymbol{\beta}$ and on its direction relative the tensor $\boldsymbol{U}$. In particular, it can be seen that the evolution equation (17) causes a competition of $\boldsymbol{\beta}$ increasing towards the value $\beta_s\boldsymbol{U}$, with the rate controlled by m_3 and thermal recovery with the rate controlled by m_4. This evolution equation causes H_T to satisfy the restriction

$$0 < 1 - \beta_s \le H_T \le 1 + \beta_s, \tag{21}$$

which ensures that the resistance $H\kappa$ to inelastic deformation rate in (9) remains positive for positive κ.

3.4. ***A scalar-based model for directional hardening.*** The scalar-based model for directional hardening is now outlined, and this model is termed “Model S” (“S” for “scalar”). A state variable β is introduced, whose evolution is given by

$$\dot{\beta} = m_3\Gamma(\beta_s U - \beta) - m_4\beta, \quad -\beta_s \le \beta \le \beta_s, \tag{22}$$

where the constants m_3, m_4 and β_s satisfy the restrictions in (17), and the Lode parameter U is defined by

$$U = \begin{cases} 0 & \text{for } \gamma_e = 0, \\ \dfrac{27\det(\boldsymbol{T}')}{2\sigma_e^3} = \dfrac{27\det\bar{\boldsymbol{B}}'_e}{16\gamma_e^3} & \text{for } \gamma_e > 0, \end{cases} \quad -1 \le U \le 1. \tag{23}$$

Next, introducing the Lode angle ϑ by the expressions

$$\sin(3\vartheta) = U, \quad -\tfrac{1}{6}\pi \le \vartheta \le \tfrac{1}{6}\pi\,, \tag{24}$$

and motivated by the simple failure surface developed in [Rubin 1991], the function H in (9) is specified by the form

$$H = H_S = 1 + \beta U. \tag{25}$$

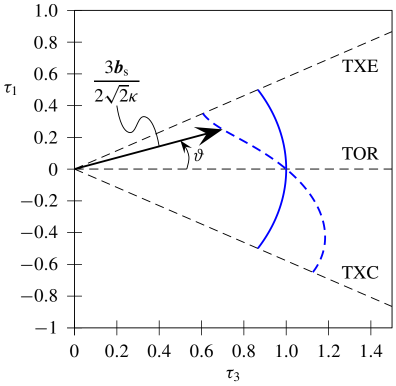

Figure 1. Normalized yield surfaces displayed in the τ_3-τ_1-plane for $\vartheta \in \left[-\frac{1}{6}\pi, \frac{1}{6}\pi\right]$: the von Mises curve (solid blue line) and an example of a curve with accumulated directional hardening (dashed blue line).

This gives the values

$$H_\mathrm{S}\big(\vartheta = \tfrac{1}{6}\pi\big) = 1 + \beta, \quad H_\mathrm{S}(\vartheta = 0) = 1, \quad H_\mathrm{S}\big(\vartheta = -\tfrac{1}{6}\pi\big) = 1 - \beta. \tag{26}$$

3.5. ***Graphical representations of models for directional hardening.*** Following [Rubin 1991], three special load cases are identified:

- triaxial extension (TXE), $U = 1$, $\vartheta = \frac{1}{6}\pi$,
- pure torsion (TOR), $U = 0$, $\vartheta = 0$,
- triaxial compression (TXC), $U = -1$, $\vartheta = -\frac{1}{6}\pi$.

Notice that the sign of ϑ is opposite to that defined in [Rubin 1991].

The loading state is characterized by $\bar{\boldsymbol{B}}'_\mathrm{e}$, whose ordered eigenvalues are denoted by $\bar{B}'_{\mathrm{e}1}$, $\bar{B}'_{\mathrm{e}2}$, and $\bar{B}'_{\mathrm{e}3}$, with $\bar{B}'_{\mathrm{e}1} \geq \bar{B}'_{\mathrm{e}2} \geq \bar{B}'_{\mathrm{e}3}$. The three load states introduced above are then characterized by

- TXE: $\bar{B}'_{\mathrm{e}1} = \frac{4}{3}\gamma_\mathrm{e}, \quad \bar{B}'_{\mathrm{e}2} = \bar{B}'_{\mathrm{e}3} = -\frac{2}{3}\gamma_\mathrm{e}$,
- TOR: $\bar{B}'_{\mathrm{e}1} = \frac{2}{\sqrt{3}}\gamma_\mathrm{e}, \quad \bar{B}'_{\mathrm{e}2} = 0, \quad \bar{B}'_{\mathrm{e}3} = -\frac{2}{\sqrt{3}}\gamma_\mathrm{e}$,
- TXC: $\bar{B}'_{\mathrm{e}1} = \bar{B}'_{\mathrm{e}2} = \frac{2}{3}\gamma_\mathrm{e}, \quad \bar{B}'_{\mathrm{e}3} = -\frac{4}{3}\gamma_\mathrm{e}$.

The yield function may be illustrated by its contour in the synoptic (or octahedral) plane, whose unit normal is given by the vector $\frac{1}{\sqrt{3}}(\boldsymbol{p}_1 + \boldsymbol{p}_2 + \boldsymbol{p}_3)$, where $\boldsymbol{p}_i$ are the orthonormal eigenvectors of $\bar{\boldsymbol{B}}'_\mathrm{e}$. Again, following [Rubin 1991], two orthogonal unit vectors in the synoptic plane are defined as

$$\bar{\boldsymbol{e}}_3 = \tfrac{1}{\sqrt{2}}(\boldsymbol{p}_1 - \boldsymbol{p}_3), \quad \bar{\boldsymbol{e}}_1 = \tfrac{1}{\sqrt{6}}(-\boldsymbol{p}_1 + 2\boldsymbol{p}_2 - \boldsymbol{p}_3). \tag{27}$$

The yield surface can be described by the vector $\boldsymbol{b}_\mathrm{s}$, defined as

$$\boldsymbol{b}_\mathrm{s} = \bar{\boldsymbol{B}}'_\mathrm{e}\big[\tfrac{1}{\sqrt{3}}(\boldsymbol{p}_1 + \boldsymbol{p}_2 + \boldsymbol{p}_3)\big] = \frac{2\sqrt{2}\,\kappa}{3}(\tau_3\bar{\boldsymbol{e}}_3 + \tau_1\bar{\boldsymbol{e}}_1), \tag{28}$$

where

$$\tau_3 = H(\vartheta)\cos\vartheta, \quad \tau_1 = H(\vartheta)\sin\vartheta. \tag{29}$$

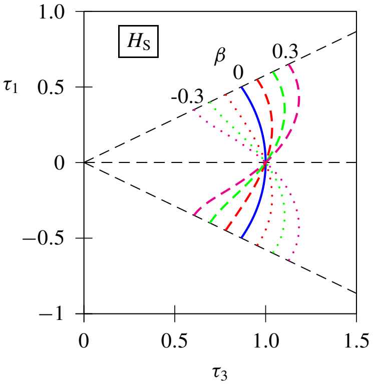

Figure 2. Yield surfaces for directional hardening displayed in the τ_3-τ_1-plane for $\vartheta \in \left[-\frac{1}{6}\pi, \frac{1}{6}\pi\right]$ for different values of β.

(It is noted that $\mu \boldsymbol{b}_\mathrm{s}/J_\mathrm{e}$ is the shearing component of the traction vector applied to the synoptic plane.) With the specification $\gamma_\mathrm{e} = \kappa H(\vartheta)$, the vector $\boldsymbol{b}_\mathrm{s}$ in (28) describes the contour of the yield surface in the synoptic plane; see Figure 1.

The state variable κ governs the isotropic expansion (or contraction) of the yield surface in the synoptic plane, whereas evolution of $\boldsymbol{\beta}$ and β cause directional hardening, i.e., different hardening for different loading modes.

The following discussion starts with the scalar-based model for directional hardening. Figure 2 shows contours of the normalized yield surface in the τ_3-τ_1-plane for different values of β. From this figure it can be seen that loading in uniaxial tension (TXE), causes an increase in β and thereby increased hardening for loading modes with $\vartheta > 0$ and softening for $\vartheta < 0$. Loading in uniaxial compression (TXC) causes the opposite tendency. For the model S, the normalized yield surface is pivoting around the yield point at $\vartheta = 0$ (TOR), which remains unaffected by directional hardening.

The yielding contour of the tensor-based model is illustrated by considering two cases of accumulated directional hardening $\boldsymbol{\beta}$: one case where the material has experienced uniaxial tension, such that

$$\beta_{ij}^{\mathrm{TXE}} = \sqrt{\tfrac{2}{3}}\beta \begin{bmatrix} 1 & 0 & 0 \\ 0 & -\frac{1}{2} & 0 \\ 0 & 0 & -\frac{1}{2} \end{bmatrix}, \tag{30}$$

and one case where the material has experienced pure torsion, i.e.,

$$\beta_{ij}^{\mathrm{TOR}} = \tfrac{1}{\sqrt{2}}\beta \begin{bmatrix} 0 & 1 & 0 \\ 1 & 0 & 0 \\ 0 & 0 & 0 \end{bmatrix}. \tag{31}$$

Above, β_{ij} denotes the Cartesian components of $\boldsymbol{\beta}$, and β is a scalar. The yield contour is then described by considering load states characterized by

$$U_{ij} = \begin{bmatrix} \xi & \zeta & 0 \\ \zeta & -\frac{1}{2}\xi & 0 \\ 0 & 0 & -\frac{1}{2}\xi \end{bmatrix}, \quad 3\xi^2 + 4\zeta^2 = 2, \tag{32}$$

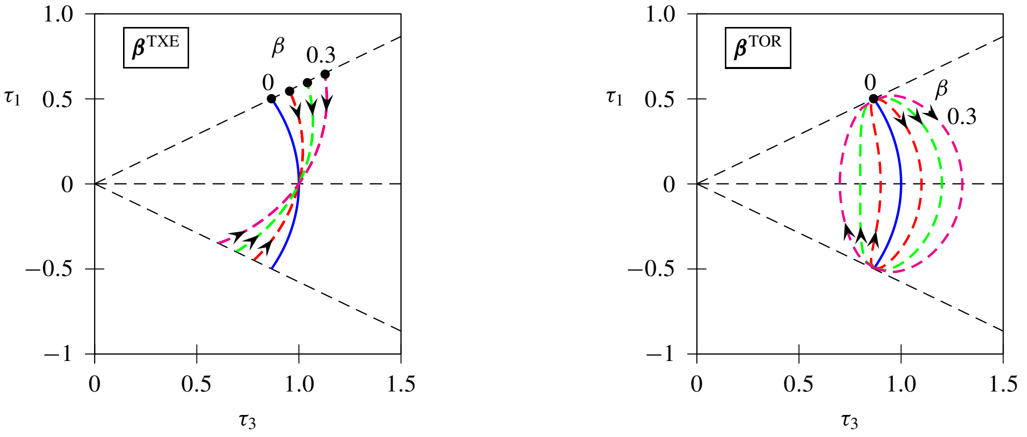

Figure 3. Yield surfaces for directional hardening predicted by the tensorial model T and displayed in the τ_3-τ_1-plane for $\vartheta \in \left[-\frac{1}{6}\pi, \frac{1}{6}\pi\right]$ for different values of β. Left: $\boldsymbol{\beta}^{\mathrm{TXE}}$. Right: $\boldsymbol{\beta}^{\mathrm{TOR}}$.

where U_{ij} are the Cartesian components of $\boldsymbol{U}$. By definition, $\boldsymbol{U} : \boldsymbol{U} = 1$, implying that (32)$_2$ must hold, and that $-\sqrt{\frac{2}{3}} \le \xi \le \sqrt{\frac{2}{3}}$ and $-\frac{1}{\sqrt{2}} \le \zeta \le \frac{1}{\sqrt{2}}$.

A loading path is now considered where the material starts in a state of uniaxial tension, passes through a state of pure torsion, then through a state of biaxial tension, then again through a state of pure torsion but with the opposite sign of the shearing, and finally back to uniaxial tension. The path of $\boldsymbol{U}$ thus passes through the points

$$\begin{aligned} &\xi = \sqrt{\tfrac{2}{3}}, && \zeta = 0 && \text{(TXE)},\\ &\xi = 0, && \zeta = \tfrac{1}{\sqrt{2}} && \text{(TOR)},\\ &\xi = -\sqrt{\tfrac{2}{3}}, && \zeta = 0 && \text{(TXC)},\\ &\xi = 0, && \zeta = -\tfrac{1}{\sqrt{2}} && \text{(TOR)},\\ &\xi = \sqrt{\tfrac{2}{3}}, && \zeta = 0 && \text{(TXE)}. \end{aligned} \tag{33}$$

The outcome is shown in Figure 3, where solutions for different values of β are shown. The black dots indicate the starting point (TXE) of the path, and the arrows indicate the direction of the path. For $\boldsymbol{\beta} = \boldsymbol{\beta}^{\mathrm{TXE}}$, the material has experienced directional hardening and softening for loads with $\vartheta > 0$ and $\vartheta < 0$, respectively, whereas the yield point for pure torsion remains unaffected. This behavior is similar to the scalar model S, as seen from Figure 2, even though the functional forms are not identical.

For a material that has experienced pure torsion, i.e., $\boldsymbol{\beta} = \boldsymbol{\beta}^{\mathrm{TOR}}$, yield contours are shown in Figure 3, right. From this figure it can be seen that torsion with a positive shearing component causes hardening in this torsion direction and softening for shearing in the opposite direction (i.e., with a negative shearing component). Yielding in TXE and TXC remains unaffected. This ability to distinguish between positive and negative shearing sets the tensor-based model apart from the scalar-based model, which is not able to make this distinction.

4. Invariance under Superposed Rigid Body Motions (SRBM)

Under Superposed Rigid Body Motions (SRBM) a quantity like the stress tensor $\boldsymbol{T}$ transforms to $\boldsymbol{T}^+$, where a superscript $(^+)$ is added to indicate the value of a quantity in the superposed configuration. In the above equations all scalars are uninfluenced by SRBM and the tensors $\boldsymbol{D}$, $\bar{\boldsymbol{B}}_\mathrm{e}$, $\boldsymbol{T}$, $\boldsymbol{\beta}$ and the Jaumann rate $\hat{\boldsymbol{\beta}}$ satisfy the transformation relations

$$\boldsymbol{D}^+ = \boldsymbol{Q}\boldsymbol{D}\boldsymbol{Q}^T, \quad \bar{\boldsymbol{B}}_\mathrm{e}^+ = \boldsymbol{Q}\bar{\boldsymbol{B}}_\mathrm{e}\boldsymbol{Q}^T, \quad \boldsymbol{T}^+ = \boldsymbol{Q}\boldsymbol{T}\boldsymbol{Q}^T, \quad \boldsymbol{\beta}^+ = \boldsymbol{Q}\boldsymbol{\beta}\boldsymbol{Q}^T, \quad \hat{\boldsymbol{\beta}}^+ = \boldsymbol{Q}\hat{\boldsymbol{\beta}}\boldsymbol{Q}^T, \tag{34}$$

where $\boldsymbol{Q}(t)$ is an arbitrary proper orthogonal tensor function of time t only. It follows that the evolution equation (3) for $\bar{\boldsymbol{B}}_\mathrm{e}$ and (17) for $\boldsymbol{\beta}$ remain form-invariant under SRBM.

5. Numerical integration algorithms

5.1. ***Preliminaries.*** This section discusses numerical algorithms to integrate the evolution equations (3) for J_e and $\bar{\boldsymbol{B}}_\mathrm{e}$ as well as the evolution equations (16) for isotropic hardening (κ), (17) for the tensorial measure $\boldsymbol{\beta}$ of directional hardening for the tensor-based model and (22) for the scalar measure β of directional hardening for the scalar-based model. These equations also use the yield function g in (9), the effective elastic distortional strain γ_e in (10), the rate of inelasticity Γ in (11) and the effective total distortional deformation rate $\dot{\varepsilon}$ in (12). Also, the constitutive equation for the Cauchy stress $\boldsymbol{T}$ is given in (7). Specifically, for the integration algorithms it is assumed that the values $J_e(t_n)$, $\bar{\boldsymbol{B}}_\mathrm{e}(t_n)$, $\kappa(t_n)$ and $\boldsymbol{\beta}(t_n)$ or $\beta(t_n)$ are known at the beginning of the time step $t = t_n$. The numerical algorithms determine the values $J_e(t_{n+1})$, $\bar{\boldsymbol{B}}_\mathrm{e}(t_{n+1})$, $\kappa(t_{n+1})$ and $\boldsymbol{\beta}(t_{n+1})$ or $\beta(t_{n+1})$ at the end of the time step $t = t_{n+1}$ with increment $\Delta t = t_{n+1} - t_n$.

Motivated by the work in [Simo 1988; Rubin and Papes 2011], recall that the relative deformation gradient $\boldsymbol{F}_\mathrm{r}$ from the time $t = t_n$, the relative dilatation J_r and the unimodular relative deformation gradient $\bar{\boldsymbol{F}}_\mathrm{r}$, satisfy the equations

$$\begin{aligned} &\dot{\boldsymbol{F}}_\mathrm{r} = \boldsymbol{L}\boldsymbol{F}_\mathrm{r}, && \boldsymbol{F}_\mathrm{r}(t_n) = \boldsymbol{I}, \\ J_\mathrm{r} = \det \boldsymbol{F}_\mathrm{r}, \quad &\dot{J}_\mathrm{r} = J_\mathrm{r}(\boldsymbol{D} : \boldsymbol{I}), && J_\mathrm{r}(t_n) = 1, \\ \bar{\boldsymbol{F}}_\mathrm{r} = J_\mathrm{r}^{-1/3}\boldsymbol{F}_\mathrm{r}, \quad &\dot{\bar{\boldsymbol{F}}}_\mathrm{r} = \boldsymbol{L}'\bar{\boldsymbol{F}}_\mathrm{r}, && \bar{\boldsymbol{F}}_\mathrm{r}(t_n) = \boldsymbol{I}. \end{aligned} \tag{35}$$

In [Rubin 2020], a strongly objective estimate $\widetilde{\boldsymbol{D}}$ of the average deformation rate over the time step was developed and is given by

$$\widetilde{\boldsymbol{D}} = \frac{1}{3\Delta t}\ln[J_r(t_{n+1})]\boldsymbol{I} + \widetilde{\boldsymbol{D}}', \quad \widetilde{\boldsymbol{D}}' = \frac{1}{2\Delta t}\left[\boldsymbol{I} - \left\{\frac{3}{\bar{\boldsymbol{B}}_\mathrm{r}^{-1}(t_{n+1}) : \boldsymbol{I}}\right\}\bar{\boldsymbol{B}}_\mathrm{r}^{-1}(t_{n+1})\right], \tag{36}$$

where $\bar{\boldsymbol{B}}_\mathrm{r}(t_{n+1}) = \bar{\boldsymbol{F}}_\mathrm{r}(t_{n+1})\bar{\boldsymbol{F}}_\mathrm{r}^\mathrm{T}(t_{n+1})$. Moreover, using this expression the average effective total distortional deformation rate $\dot{\varepsilon}$ during the time step is approximated by

$$\dot{\varepsilon} \approx \dot{\tilde{\varepsilon}} = \sqrt{\tfrac{2}{3}\widetilde{\boldsymbol{D}}' : \widetilde{\boldsymbol{D}}'}. \tag{37}$$

5.2. ***Integration of J_e, $\bar{\boldsymbol{B}}_\mathrm{e}$, κ, and $\varepsilon_\mathrm{p}^\mathrm{e}$.*** It is recalled from [Rubin and Cardiff 2017] that the exact solution for J_e is given by

$$J_\mathrm{e}(t_{n+1}) = J_\mathrm{r}(t_{n+1})J_\mathrm{e}(t_n). \tag{38}$$

Also, using the elastic trial $\bar{\boldsymbol{B}}_{\mathrm{e}}^{*}$

$$\bar{\boldsymbol{B}}_{\mathrm{e}}^{*} = \bar{\boldsymbol{F}}_{\mathrm{r}} \bar{\boldsymbol{B}}_{\mathrm{e}}(t_n) \bar{\boldsymbol{F}}_{\mathrm{r}}^{\mathrm{T}}, \tag{39}$$

it can be shown that its deviatoric part $\bar{\boldsymbol{B}}_{\mathrm{e}}^{\prime *}$ satisfies the evolution equation

$$\dot{\bar{\boldsymbol{B}}}_{\mathrm{e}}^{\prime *} = \boldsymbol{L}^{\prime} \bar{\boldsymbol{B}}_{\mathrm{e}}^{*} + \bar{\boldsymbol{B}}_{\mathrm{e}}^{*} \boldsymbol{L}^{\prime T} - \tfrac{2}{3}(\bar{\boldsymbol{B}}_{\mathrm{e}}^{\prime *} : \boldsymbol{D}^{\prime})\boldsymbol{I}. \tag{40}$$

Also, taking the deviatoric part of the evolution equation (3) requires $\bar{\boldsymbol{B}}_{\mathrm{e}}^{\prime}$ to satisfy the evolution equation

$$\dot{\bar{\boldsymbol{B}}}_{\mathrm{e}}^{\prime} = \boldsymbol{L}^{\prime} \bar{\boldsymbol{B}}_{\mathrm{e}} + \bar{\boldsymbol{B}}_{\mathrm{e}} \boldsymbol{L}^{\prime T} - \tfrac{2}{3}(\bar{\boldsymbol{B}}_{\mathrm{e}}^{\prime} : \boldsymbol{D}^{\prime})\boldsymbol{I} - \Gamma \bar{\boldsymbol{B}}_{\mathrm{e}}^{\prime}. \tag{41}$$

Then, approximating this equation by

$$\dot{\bar{\boldsymbol{B}}}_{e}^{\prime} = \dot{\bar{\boldsymbol{B}}}_{\mathrm{e}}^{\prime *} - \Gamma \bar{\boldsymbol{B}}_{\mathrm{e}}^{\prime}, \tag{42}$$

and using a backward Euler approximation of the derivative yields the solution

$$\bar{\boldsymbol{B}}_{\mathrm{e}}^{\prime}(t_{n+1}) = \frac{\bar{\boldsymbol{B}}_{\mathrm{e}}^{\prime *}(t_{n+1})}{1 + \Delta\Gamma} = \lambda \bar{\boldsymbol{B}}_{\mathrm{e}}^{\prime *}(t_{n+1}), \tag{43}$$

where $\Delta\Gamma$ is defined by

$$\Delta\Gamma = \Delta t \Gamma(t_{n+1}), \tag{44}$$

and $\Gamma(t_{n+1})$ is the value of function Γ defined in (11) at the end of the time step. It can be seen that the solution (43) is similar to the radial return algorithm proposed by [Wilkins 1963] with the final value of elastic distortional deformation being a scalar time its elastic trial value. Once $\bar{\boldsymbol{B}}_{\mathrm{e}}^{\prime}(t_{n+1})$ is known, the value $\bar{\boldsymbol{B}}_{\mathrm{e}}(t_{n+1})$ can be determined by solving the cubic equation

$$\det\left[\tfrac{1}{3}\alpha_1 \boldsymbol{I} + \bar{\boldsymbol{B}}_{\mathrm{e}}^{\prime}(t_{n+1})\right] = 1 \tag{45}$$

for α_1, as discussed in [Rubin and Attia 1996; Hollenstein et al. 2013].

The evolution equation (16) for the isotropic hardening variable κ can be integrated using an backward Euler estimate of the derivative to obtain

$$\kappa(t_{n+1}) = \frac{\kappa(t_n) + m_1 \Delta\Gamma \kappa_{\mathrm{s}} + \Delta t m_2 \kappa_{\mathrm{a}}}{1 + m_1 \Delta\Gamma + \Delta t m_2}. \tag{46}$$

Also, the equivalent inelastic strain is determined by integrating the evolution equation

$$\varepsilon_{\mathrm{p}}(t_{n+1}) = \varepsilon_{\mathrm{p}}(t_n) + \tfrac{2}{3} \Delta\Gamma \lambda \gamma_{\mathrm{e}}^{*}. \tag{47}$$

5.3. *Integration of $\boldsymbol{\beta}$.* Using the Jaumann derivative (18), the evolution equation for the deviatoric tensor $\boldsymbol{\beta}$ can be written in the form

$$\dot{\boldsymbol{\beta}} = \boldsymbol{W}\boldsymbol{\beta} + \boldsymbol{\beta}\boldsymbol{W}^{T} + m_3 \Gamma(\beta_{\mathrm{s}} \boldsymbol{U} - \boldsymbol{\beta}) - m_4 \boldsymbol{\beta}. \tag{48}$$

Now, following the work in [Rubin 2020], it is convenient to introduce the elastic trial value $\boldsymbol{\beta}^{*}$, which is the solution for $\boldsymbol{\beta}$ in the absence of inelasticity and thermal recovery, i.e.,

$$\dot{\boldsymbol{\beta}}^{*} = \boldsymbol{W}\boldsymbol{\beta}^{*} + \boldsymbol{\beta}^{*}\boldsymbol{W}^{T} = \boldsymbol{L}\boldsymbol{\beta}^{*} + \boldsymbol{\beta}^{*}\boldsymbol{L}^{T} - \tfrac{2}{3}(\boldsymbol{\beta}^{*} : \boldsymbol{D})\boldsymbol{I} - \boldsymbol{R}, \quad \boldsymbol{\beta}^{*}(t_n) = \boldsymbol{\beta}(t_n), \tag{49}$$

with

$$\boldsymbol{R} = \boldsymbol{R}(\boldsymbol{\beta}^*, \boldsymbol{D}) = \boldsymbol{D}\boldsymbol{\beta}^* + \boldsymbol{\beta}^*\boldsymbol{D} - \tfrac{2}{3}(\boldsymbol{\beta}^* : \boldsymbol{D})\boldsymbol{I}. \tag{50}$$

Equation (48) can then be approximated by

$$\dot{\boldsymbol{\beta}} \approx \dot{\boldsymbol{\beta}}^* + m_3\Gamma(\beta_\mathrm{s}\boldsymbol{U} - \boldsymbol{\beta}) - m_4\boldsymbol{\beta}\,. \tag{51}$$

To solve (49), it is also convenient to introduce the auxiliary deviatoric tensor $\bar{\boldsymbol{\beta}}'$, which satisfies the equations

$$\bar{\boldsymbol{\beta}} = \boldsymbol{F}_\mathrm{r}\boldsymbol{\beta}(t_n)\boldsymbol{F}_\mathrm{r}^\mathrm{T}, \quad \bar{\boldsymbol{\beta}}'(t_n) = \boldsymbol{\beta}(t_n), \quad \dot{\bar{\boldsymbol{\beta}}}' = \boldsymbol{L}\bar{\boldsymbol{\beta}}' + \bar{\boldsymbol{\beta}}'\boldsymbol{L}^\mathrm{T} - \tfrac{2}{3}(\bar{\boldsymbol{\beta}}' : \boldsymbol{D})\boldsymbol{I}, \tag{52}$$

and rewrite (49) in the approximate form

$$\dot{\boldsymbol{\beta}}^* \approx \dot{\bar{\boldsymbol{\beta}}}' - \boldsymbol{R}(\bar{\boldsymbol{\beta}}', \boldsymbol{D}). \tag{53}$$

Using a backward Euler approximation of the derivatives, (53) is integrated to obtain

$$\boldsymbol{\beta}^*(t_{n+1}) \approx \alpha(\bar{\boldsymbol{\beta}}'(t_{n+1}) - \Delta\boldsymbol{R}), \quad \Delta\boldsymbol{R} = \Delta t\,\boldsymbol{R}(\bar{\boldsymbol{\beta}}'(t_{n+1}), \widetilde{\boldsymbol{D}}), \alpha = \frac{|\boldsymbol{\beta}(t_n)|}{|\bar{\boldsymbol{\beta}}'(t_{n+1}) - \Delta\boldsymbol{R}|}, \tag{54}$$

where the scalar α is a correction factor that ensures that the elastic trial $\boldsymbol{\beta}^*(t_{n+1})$ is consistent with a pure rotation, since it has the same magnitude as $\boldsymbol{\beta}(t_n)$.

Also, with the help of (20) and (43) it can be shown that

$$\boldsymbol{U}(t_{n+1}) = \boldsymbol{U}^* = \frac{\bar{\boldsymbol{B}}_\mathrm{e}'^*}{|\bar{\boldsymbol{B}}_\mathrm{e}'^*|} = \sqrt{\tfrac{3}{8}}\,\frac{\bar{\boldsymbol{B}}_\mathrm{e}'^*}{\gamma_\mathrm{e}^*}, \tag{55}$$

with

$$\gamma_\mathrm{e}^* = \tfrac{1}{2}\sqrt{\tfrac{3}{2}\bar{\boldsymbol{B}}_\mathrm{e}'^* : \bar{\boldsymbol{B}}_\mathrm{e}'^*}. \tag{56}$$

Finally, using a backward Euler approximation of the derivative in (51), the value $\boldsymbol{\beta}(t_{n+1})$ is determined by

$$\boldsymbol{\beta}(t_{n+1}) = \frac{\boldsymbol{\beta}^*(t_{n+1}) + m_3\beta_\mathrm{s}\Delta\Gamma\boldsymbol{U}(t_{n+1})}{1 + m_3\Delta\Gamma + m_4\Delta t}, \tag{57}$$

where $\Delta\Gamma$ is defined by (44).

5.4. ***Integration of $\boldsymbol{\beta}$.*** Using the fact that the Lode parameter U defined in (23) has the same value at the end of the time step as its value based on the elastic trial solution

$$U(\bar{\boldsymbol{B}}_\mathrm{e}'(t_{n+1})) = U^*(\bar{\boldsymbol{B}}_\mathrm{e}'^*) = \frac{27\det\bar{\boldsymbol{B}}_\mathrm{e}'^*}{16\gamma_\mathrm{e}^{*3}}, \tag{58}$$

the evolution equation (22) for the directional hardening parameter β can be integrated to obtain

$$\beta(t_{n+1}) = \frac{\beta(t_n) + m_3\beta_\mathrm{s}\Delta\Gamma U(t_{n+1})}{1 + m_3\Delta\Gamma + m_4\Delta t}. \tag{59}$$

5.5. *Determination of* $\Delta\Gamma$. The numerical approximations of the state variables above depend on the increment $\Delta\Gamma$, which has not been specified yet. If $\gamma_e^* \le \kappa^* H^*$, where κ^* and H^* denote the values of $\kappa(t_{n+1})$ and $H(t_{n+1})$ evaluated for $\Delta\Gamma = 0$, then the step is elastic and $\Delta\Gamma = 0$ holds. On the other hand, if $\gamma_e^* > \kappa^* H^*$, then the step is inelastic, and $\Delta\Gamma$ needs to be determined by solving (44), which implicitly defines $\Delta\Gamma$, since the right-hand side of (44) is a function of the updated state variables that in turn depend on $\Delta\Gamma$. In the present work, (44) is solved through a Newton–Raphson scheme.

5.6. *Strong objectivity.* These numerical estimates $J_e(t_{n+1})$, $\bar{\boldsymbol{B}}_{\mathrm{e}}(t_{n+1})$, $\kappa(t_{n+1})$, $\boldsymbol{\beta}(t_{n+1})$ and $\beta(t_{n+1})$ are strongly objective in the sense discussed in [Papes 2012] and [Rubin and Papes 2011] since they satisfy the same transformation under SRBM as the exact values

$$J_e^+(t_{n+1}) = J_e(t_{n+1}), \quad \bar{\boldsymbol{B}}_{\mathrm{e}}^+(t_{n+1}) = \boldsymbol{Q}\bar{\boldsymbol{B}}_{\mathrm{e}}(t_{n+1})\boldsymbol{Q}^T, \tag{60}$$

$$\kappa^+(t_{n+1}) = \kappa(t_{n+1}), \quad \boldsymbol{\beta}^+(t_{n+1}) = \boldsymbol{Q}\boldsymbol{\beta}(t_{n+1})\boldsymbol{Q}^T, \quad \beta^+(t_{n+1}) = \beta(t_{n+1}), \tag{61}$$

for arbitrary SRBM.

5.7. *Algorithmic tangent stiffness.* In the derivation of the algorithmic (consistent) tangent stiffness below, entities are understood as pertaining to the end of the time step, i.e., $t = t_{n+1}$, unless otherwise specified. To simplify the notation, two tensor operators are introduced:

$$(\boldsymbol{Q} \otimes \boldsymbol{R})_{ijkl} = Q_{ij} R_{kl}, \tag{62}$$

$$(\boldsymbol{Q} \oplus \boldsymbol{R})_{ijkl} = \tfrac{1}{2}(Q_{ik}R_{jl} + R_{il}Q_{jk}). \tag{63}$$

The Kirchhoff stress is given by $\boldsymbol{\tau} = J_{\mathrm{e}}\boldsymbol{T}$ and is a function of $\boldsymbol{F}_{\mathrm{r}}$. The variation of $\boldsymbol{\tau}$ is given by

$$\delta\boldsymbol{\tau} = \frac{\partial\boldsymbol{\tau}}{\partial\boldsymbol{F}_{\mathrm{r}}} : \delta\boldsymbol{F}_{\mathrm{r}} = \left[\left(\frac{\partial\boldsymbol{\tau}}{\partial\boldsymbol{F}_{\mathrm{r}}}\right)\boldsymbol{F}_{\mathrm{r}}^{\mathrm{T}}\right] : (\delta\boldsymbol{F}_{\mathrm{r}}\boldsymbol{F}_{\mathrm{r}}^{-1}). \tag{64}$$

The consistent tangent modulus, $\mathbb{C}$, is then identified as

$$\mathbb{C} = \frac{1}{J_e}\left(\frac{\partial\boldsymbol{\tau}}{\partial\boldsymbol{F}_{\mathrm{r}}}\right)\boldsymbol{F}_{\mathrm{r}}^{\mathrm{T}} = \frac{1}{J_{\mathrm{e}}}\left[K\boldsymbol{I} \otimes \frac{\partial J_{\mathrm{e}}}{\partial\boldsymbol{F}_{\mathrm{r}}} + \mu\left(\frac{\partial\bar{\boldsymbol{B}}_{\mathrm{e}}'}{\partial\boldsymbol{F}_{\mathrm{r}}}\right)\right]\boldsymbol{F}_{\mathrm{r}}^{\mathrm{T}}. \tag{65}$$

A few simplifications are made when deriving the consistent tangent modulus. In practice, the factor α in (54) is close to unity, and the influence of α on the algorithmic stiffness is therefore ignored. Furthermore, the approximation of $\boldsymbol{D}$ is replaced by the simpler expression [Hollenstein et al. 2013]

$$\boldsymbol{D} \approx \frac{1}{2\Delta t}(\boldsymbol{B}_{\mathrm{r}} - \boldsymbol{I}), \tag{66}$$

where $\boldsymbol{B}_{\mathrm{r}} = \boldsymbol{F}_{\mathrm{r}}\boldsymbol{F}_{\mathrm{r}}^{\mathrm{T}}$. However, the forms (36) and (54) are used in evaluating the constitutive equations.

Recalling that the current value of J_{e} is given by $J_{\mathrm{e}} = J_{\mathrm{e}}(t_1)J_{\mathrm{r}}$, it follows that

$$\frac{\partial J_{\mathrm{e}}}{\partial\boldsymbol{F}_{\mathrm{r}}}\boldsymbol{F}_{\mathrm{r}}^{\mathrm{T}} = J_{\mathrm{e}}(t_1)\frac{\partial J_{\mathrm{r}}}{\partial\boldsymbol{F}_{\mathrm{r}}}\boldsymbol{F}_{\mathrm{r}}^{\mathrm{T}} = J_{\mathrm{e}}(t_1)J_{\mathrm{r}}\boldsymbol{F}_{\mathrm{r}}^{-\mathrm{T}}\boldsymbol{F}_{\mathrm{r}}^{\mathrm{T}} = J_{\mathrm{e}}\boldsymbol{I}. \tag{67}$$

The second term in (65) is given by

$$\left(\frac{\partial\bar{\boldsymbol{B}}_{\mathrm{e}}'}{\partial\boldsymbol{F}_{\mathrm{r}}}\right)\boldsymbol{F}_{\mathrm{r}}^{\mathrm{T}} = \partial(\lambda\bar{\boldsymbol{B}}_{\mathrm{e}}'^{*})\partial\boldsymbol{F}_{\mathrm{r}}\boldsymbol{F}_{\mathrm{r}}^{\mathrm{T}} = -\lambda^2\bar{\boldsymbol{B}}_{\mathrm{e}}'^{*} \otimes \left(\frac{\partial(\Delta\Gamma)}{\partial\boldsymbol{F}_{\mathrm{r}}}\boldsymbol{F}_{\mathrm{r}}^{\mathrm{T}}\right) + \lambda\left(\frac{\partial\bar{\boldsymbol{B}}_{\mathrm{e}}'^{*}}{\partial\boldsymbol{F}_{\mathrm{r}}}\right)\boldsymbol{F}_{\mathrm{r}}^{\mathrm{T}}. \tag{68}$$

For the last derivative in the expression above, it is first noted that

$$\left(\frac{\partial \bar{\boldsymbol{B}}_{\mathrm{e}}^{*}}{\partial \boldsymbol{F}_{\mathrm{r}}}\right)=-\tfrac{2}{3}\bar{\boldsymbol{B}}_{\mathrm{e}}^{*}\otimes \boldsymbol{F}_{\mathrm{r}}^{-\mathrm{T}}+\frac{1}{J_{\mathrm{r}}^{2/3}}\frac{\partial[\boldsymbol{F}_{\mathrm{r}}\bar{\boldsymbol{B}}_{\mathrm{e}}(t_1)\boldsymbol{F}_{\mathrm{r}}^{\mathrm{T}}]}{\partial \boldsymbol{F}_{\mathrm{r}}}, \tag{69}$$

and that

$$\frac{\partial[\boldsymbol{F}_{\mathrm{r}}\bar{\boldsymbol{B}}_{\mathrm{e}}(t_1)\boldsymbol{F}_{\mathrm{r}}^{\mathrm{T}}]}{\partial \boldsymbol{F}_{\mathrm{r}}}=2(\boldsymbol{I}\oplus \boldsymbol{F}_{\mathrm{r}})\bar{\boldsymbol{B}}_{\mathrm{e}}(t_1). \tag{70}$$

A fourth-order tensor $\mathbb{D}_1$ is then defined as

$$\mathbb{D}_1=\left(\frac{\partial \bar{\boldsymbol{B}}_{\mathrm{e}}^{\prime *}}{\partial \boldsymbol{F}_{\mathrm{r}}}\right)\boldsymbol{F}_{\mathrm{r}}^{\mathrm{T}}=2\boldsymbol{I}\oplus \bar{\boldsymbol{B}}_{\mathrm{e}}^{*}-\tfrac{2}{3}(\boldsymbol{I}\otimes \bar{\boldsymbol{B}}_{\mathrm{e}}^{*}+\bar{\boldsymbol{B}}_{\mathrm{e}}^{*}\otimes \boldsymbol{I})+\tfrac{2}{9}(\bar{\boldsymbol{B}}_{\mathrm{e}}^{*}:\boldsymbol{I})\boldsymbol{I}\otimes \boldsymbol{I}. \tag{71}$$

Differentiation of $\Delta\Gamma$ in (44) yields

$$\left(1+\lambda\zeta_1+\frac{\zeta_1\zeta_2}{\kappa}\right)\delta(\Delta\Gamma)=\frac{\Delta\Gamma}{\dot{\varepsilon}}\delta\dot{\varepsilon}+\frac{\zeta_1}{\gamma_{\mathrm{e}}^{*}}\delta\gamma_{\mathrm{e}}^{*}-\frac{\zeta_1}{H}\delta H, \tag{72}$$

where

$$\delta\dot{\varepsilon}=\frac{2}{3\dot{\varepsilon}}\boldsymbol{D}':\left(\frac{\partial \boldsymbol{D}'}{\partial \boldsymbol{F}_{\mathrm{r}}}\right):\delta \boldsymbol{F}_{\mathrm{r}}, \tag{73}$$

$$\left(\frac{\partial \boldsymbol{D}'}{\partial \boldsymbol{F}_{\mathrm{r}}}\right)=\frac{1}{\Delta t}\big(\boldsymbol{I}\oplus \boldsymbol{F}_{\mathrm{r}}-\tfrac{1}{3}\boldsymbol{I}\otimes \boldsymbol{F}_{\mathrm{r}}\big), \tag{74}$$

$$\delta\gamma_{\mathrm{e}}^{*}=\frac{3}{8\gamma_{\mathrm{e}}^{*}}\bar{\boldsymbol{B}}_{\mathrm{e}}^{\prime *}:\left(\frac{\partial \bar{\boldsymbol{B}}_{\mathrm{e}}^{\prime *}}{\partial \boldsymbol{F}_{\mathrm{r}}}\right):\delta \boldsymbol{F}_{\mathrm{r}}, \tag{75}$$

and

$$\zeta_1=\frac{b_1\dot{\varepsilon}\Delta t\kappa H}{\gamma_{\mathrm{e}}},\qquad \zeta_2=\frac{\mathrm{d}\kappa}{\mathrm{d}(\Delta\Gamma)}=\frac{m_1(\kappa_{\mathrm{s}}-\kappa)}{1+m_1\Delta\Gamma+m_2\Delta t}. \tag{76}$$

For the scalar model (model S) it follows that

$$\delta H=\delta H_{\mathrm{S}}=U\delta\beta+\beta\delta U=U\zeta_3\delta(\Delta\Gamma)+(\beta+\zeta_4 U)\delta U, \tag{77}$$

where

$$\zeta_3=\frac{\mathrm{d}\beta}{\mathrm{d}(\Delta\Gamma)}=\frac{m_3(\beta_{\mathrm{s}}U-\beta)}{1+m_3\Delta\Gamma+m_4\Delta t},\qquad \zeta_4=\frac{m_3\beta_{\mathrm{s}}\Delta\Gamma}{1+m_3\Delta\Gamma+m_4\Delta t}, \tag{78}$$

and

$$\delta U=\boldsymbol{M}_{\mathrm{S}}:\left(\frac{\partial \bar{\boldsymbol{B}}_{\mathrm{e}}^{\prime *}}{\partial \boldsymbol{F}_{\mathrm{r}}}\right):\delta \boldsymbol{F}_{\mathrm{r}}, \tag{79}$$

where

$$\boldsymbol{M}_{\mathrm{S}}=U\left(\bar{\boldsymbol{B}}_{\mathrm{e}}^{\prime *-1}-\frac{9}{8\gamma_{\mathrm{e}}^{*2}}\bar{\boldsymbol{B}}_{\mathrm{e}}^{\prime *}\right). \tag{80}$$

For the tensorial model (model T) it follows that

$$\delta H=\delta H_{\mathrm{T}}=\boldsymbol{U}:\delta\boldsymbol{\beta}+\boldsymbol{\beta}:\delta\boldsymbol{U}=\zeta_5\boldsymbol{U}:\delta\boldsymbol{\beta}^{*}+\boldsymbol{U}:\boldsymbol{M}_{\mathrm{T}}\delta(\Delta\Gamma)+(\boldsymbol{\beta}+\zeta_4\boldsymbol{U}):\delta\boldsymbol{U}, \tag{81}$$

where

$$\zeta_5=\frac{1}{1+m_3\Delta\Gamma+m_4\Delta t},\qquad \boldsymbol{M}_{\mathrm{T}}=\frac{m_3(\beta_{\mathrm{s}}\boldsymbol{U}-\boldsymbol{\beta})}{1+m_3\Delta\Gamma+m_4\Delta t}. \tag{82}$$

Moreover, we have

$$\delta\boldsymbol{\beta}^* = \Big(\frac{\partial\boldsymbol{\beta}^*}{\partial\boldsymbol{F}_{\rm r}}\Big) : \delta\boldsymbol{F}_{\rm r},$$

$$\Big(\frac{\partial\boldsymbol{\beta}^*}{\partial\boldsymbol{F}_{\rm r}}\Big) = \big(2\boldsymbol{I} - \tfrac{1}{2}\boldsymbol{B}_{\rm r}\big)\Big(\frac{\partial\bar{\boldsymbol{\beta}}'}{\partial\boldsymbol{F}_{\rm r}}\Big) + \tfrac{1}{3}\boldsymbol{I}\otimes\Big[\boldsymbol{B}_{\rm r} : \Big(\frac{\partial\bar{\boldsymbol{\beta}}'}{\partial\boldsymbol{F}_{\rm r}}\Big) + 2\bar{\boldsymbol{\beta}}'\boldsymbol{F}_{\rm r}\Big] - \boldsymbol{I}\oplus(\bar{\boldsymbol{\beta}}'\boldsymbol{F}_{\rm r}) - \bar{\boldsymbol{\beta}}'\oplus\boldsymbol{F}_{\rm r}, \tag{83}$$

$$\Big(\frac{\partial\bar{\boldsymbol{\beta}}'}{\partial\boldsymbol{F}_{\rm r}}\Big) = 2\big(\boldsymbol{I}\oplus\boldsymbol{F}_{\rm r} - \tfrac{1}{3}\boldsymbol{I}\otimes\boldsymbol{F}_{\rm r}\big)\boldsymbol{\beta}(t_n), \tag{84}$$

$$\delta\boldsymbol{U} = \mathbb{M}_{\rm T} : \Big(\frac{\partial\bar{\boldsymbol{B}}_{\rm e}'^*}{\partial\boldsymbol{F}_{\rm r}}\Big) : \delta\boldsymbol{F}_{\rm r}, \tag{85}$$

$$\mathbb{M}_{\rm T} = \sqrt{\frac{3}{8}}\frac{1}{\gamma_{\rm e}^*}\Big(\mathbb{I} - \frac{3}{8\gamma_{\rm e}^{*2}}\bar{\boldsymbol{B}}_{\rm e}'^*\otimes\bar{\boldsymbol{B}}_{\rm e}'^*\Big), \tag{86}$$

where $\mathbb{I} = \boldsymbol{I}\oplus\boldsymbol{I}$ is the fourth-order unit tensor. This finally gives

$$\frac{\partial(\Delta\Gamma)}{\partial\boldsymbol{F}_{\rm r}}\boldsymbol{F}_{\rm r}^{\rm T} = \boldsymbol{H} = \frac{\kappa}{\zeta_6}\Big\{\frac{2\Delta\Gamma H\gamma_{\rm e}^{*2}}{3}\boldsymbol{D}' : \mathbb{D}_2 + \zeta_1\dot{\varepsilon}^2\Big[\frac{3H}{8}\bar{\boldsymbol{B}}_{\rm e}'^* - \gamma_{\rm e}^{*2}\boldsymbol{N}_{1,{\rm S/T}}\Big] : \mathbb{D}_1 - \boldsymbol{N}_{2,{\rm S/T}}\Big\}, \tag{87}$$

where

$$\zeta_6 = \dot{\varepsilon}^2\gamma_{\rm e}^{*2}(\kappa H + \zeta_1\lambda\kappa H + \zeta_1\zeta_2 H + N_{\rm S/T}), \tag{88}$$

$$\mathbb{D}_2 = \Big(\frac{\partial\boldsymbol{D}'}{\partial\boldsymbol{F}_{\rm r}}\Big)\boldsymbol{F}_{\rm r}^{\rm T} = \frac{1}{\Delta t}\big[\boldsymbol{I}\oplus\boldsymbol{B}_{\rm r} - \tfrac{1}{3}\boldsymbol{I}\otimes\boldsymbol{B}_{\rm r}\big], \tag{89}$$

$$N_{\rm S} = \zeta_1\zeta_3\kappa U, \quad N_{\rm T} = \zeta_1\kappa\boldsymbol{U} : \boldsymbol{M}_{\rm T}, \tag{90}$$

$$\boldsymbol{N}_{1,{\rm S}} = (\beta + \zeta_4 U)\boldsymbol{M}_{\rm S}, \quad \boldsymbol{N}_{1,{\rm T}} = (\boldsymbol{\beta} + \zeta_4\boldsymbol{U}) : \mathbb{M}_{\rm T}, \tag{91}$$

$$\boldsymbol{N}_{2,{\rm S}} = \boldsymbol{0}, \quad \boldsymbol{N}_{2,{\rm T}} = \zeta_1\zeta_5\dot{\varepsilon}^2\gamma_{\rm e}^{*2}\boldsymbol{U} : \mathbb{D}_3, \tag{92}$$

$$\begin{aligned}\mathbb{D}_3 = \Big(\frac{\partial\boldsymbol{\beta}^*}{\partial\boldsymbol{F}_{\rm r}}\Big)\boldsymbol{F}_{\rm r}^{\rm T} &= 4\big(\boldsymbol{I}\oplus\bar{\boldsymbol{\beta}} - \tfrac{1}{3}\boldsymbol{I}\otimes\bar{\boldsymbol{\beta}}\big) + \boldsymbol{I}\oplus(\bar{\boldsymbol{\beta}}'\boldsymbol{B}_{\rm r} + \boldsymbol{B}_{\rm r}\bar{\boldsymbol{\beta}}') \\ &\quad + \bar{\boldsymbol{\beta}}\oplus\boldsymbol{B}_{\rm r} + \boldsymbol{B}_{\rm r}\oplus\bar{\boldsymbol{\beta}} - \tfrac{2}{3}\boldsymbol{B}_{\rm r}\otimes\bar{\boldsymbol{\beta}} + \tfrac{2}{3}\boldsymbol{I}\otimes(\boldsymbol{B}_{\rm r}'\bar{\boldsymbol{\beta}} + \bar{\boldsymbol{\beta}}'\boldsymbol{B}_{\rm r}).\end{aligned} \tag{93}$$

Above, the entities $(\bullet)_{\rm S/T}$ take on the values $(\bullet)_{\rm S}$ and $(\bullet)_{\rm T}$ for model S and model T, respectively. It then follows that

$$\Big(\frac{\partial\bar{\boldsymbol{B}}_{\rm e}'}{\partial\boldsymbol{F}_{\rm r}}\Big)\boldsymbol{F}_{\rm r}^{\rm T} = \mathbb{H} = \lambda\Big(\frac{\partial\bar{\boldsymbol{B}}_{\rm e}'^*}{\partial\boldsymbol{F}_{\rm r}}\Big)\boldsymbol{F}_{\rm r}^{\rm T} - \lambda^2\bar{\boldsymbol{B}}_{\rm e}'^*\otimes\frac{\partial(\Delta\Gamma)}{\partial\boldsymbol{F}_{\rm r}}\boldsymbol{F}_{\rm r}^{\rm T} = \lambda\mathbb{D}_1 - \lambda^2\bar{\boldsymbol{B}}_{\rm e}'^*\otimes\boldsymbol{H}. \tag{94}$$

The total mechanical stiffness is then given by

$$\mathbb{C} = K\boldsymbol{I}\otimes\boldsymbol{I} + \frac{\mu}{J_{\rm e}}\mathbb{H}. \tag{95}$$

6. Examples

6.1. ***Prerequisites.*** The stress response and evolution of relevant state variables for different loading paths and cases are now considered. The components, T_{ij} of the stress tensor $\boldsymbol{T}$ referred to the fixed rectangular Cartesian base vectors $\boldsymbol{e}_i$ are defined by

$$T_{ij} = \boldsymbol{T} : \boldsymbol{e}_i \otimes \boldsymbol{e}_j, \tag{96}$$

with $\boldsymbol{a} \otimes \boldsymbol{b}$ denoting the tensor product between the two vectors $\boldsymbol{a}$ and $\boldsymbol{b}$. The following examples consider steel at room temperature with thermal recovery inactive so that

$$m_2 = m_4 = 0. \tag{97}$$

In addition, the material is assumed to be initially in a zero-stress fully annealed state with the initial conditions specified by:

$$J_\mathrm{e}(0) = 1, \quad \bar{\boldsymbol{B}}_\mathrm{e}(0) = \boldsymbol{I}, \quad \kappa(0) = \kappa_\mathrm{a}, \quad \boldsymbol{\beta}(0) = \boldsymbol{0}, \quad \beta(0) = 0. \tag{98}$$

6.2. ***Cyclic uniaxial stress loading — comparison with experiments.*** For cyclic uniaxial stress loading, the deformation gradient $\boldsymbol{F}$ is specified by

$$\boldsymbol{F} = a\boldsymbol{e}_1 \otimes \boldsymbol{e}_1 + b(\boldsymbol{e}_2 \otimes \boldsymbol{e}_2 + \boldsymbol{e}_3 \otimes \boldsymbol{e}_3), \tag{99}$$

where a is the stretch in the loading direction and b is the lateral stretch. The axial stretch a is a specified function of time only and the lateral stretch b is determined by the lateral boundary condition

$$T_{22} = 0, \tag{100}$$

where it is noted that $T_{33} = T_{22}$ for this deformation.

Figure 4 considers uniaxial tension to different extensions $a - 1$ followed by reverse loadings into compression. The experimental data for austenitic stainless steel (316L) at room temperature is taken from [Choteau et al. 2005] and is denoted by symbols. It should be noted that for this case of uniaxial stress, models T and S predict exactly the same response for the same material constants. The following model material constants

$$\begin{aligned} &\mu = 69\,\mathrm{GPa}, \quad K = 167\,\mathrm{GPa}, \quad b_1 = 2.5 \cdot 10^3, \quad m_1 = 0.0017, \\ &\kappa_a = 0.0012, \quad \kappa_s = 0.01, \quad m_3 = 0.15, \quad \beta_s = 0.35, \end{aligned} \tag{101}$$

have been calibrated, and the results in Figure 4 show excellent comparison of model predictions to the experimental data.

6.3. ***Cyclic loading with simple deformation modes.*** For the remaining examples in this paper, the material constants are specified by

$$\begin{aligned} &\mu = 77\,\mathrm{GPa}, \quad K = 167\,\mathrm{GPa}, \quad b_1 = 10^5, \quad m_1 = 0.001, \\ &\kappa_a = 0.002, \quad \kappa_s = 0.012, \quad m_3 = 0.2, \quad \beta_s = 0.3. \end{aligned} \tag{102}$$

Also, in this subsection attention is limited to isochoric deformation with the deformation gradient $\boldsymbol{F}$ specified by

$$\boldsymbol{F} = a\boldsymbol{e}_1 \otimes \boldsymbol{e}_1 + \left(a\gamma\boldsymbol{e}_1 + \frac{1}{\sqrt{a}}\boldsymbol{e}_2\right) \otimes \boldsymbol{e}_2 + \frac{1}{\sqrt{a}}\boldsymbol{e}_3 \otimes \boldsymbol{e}_3, \quad J_\mathrm{e} = \det \boldsymbol{F} = 1, \tag{103}$$

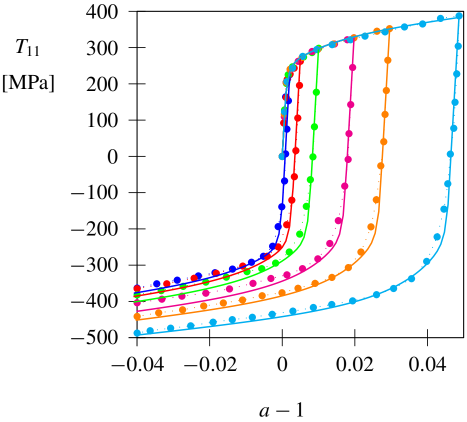

Figure 4. Material response for cyclic uniaxial stress with loading up to different maximum extensions $a-1$ followed by reversed loading; data from [Choteau et al. 2005] (symbols) for austenitic stainless steel (316L) together with the calibrated model responses (solid lines).

where a and γ are functions of time only. Using this expression it can be shown that the rate of deformation tensor $\boldsymbol{D}$ and the spin tensor $\boldsymbol{W}$ can be expressed in the forms

$$\begin{aligned} \boldsymbol{D} &= \frac{\dot{a}}{a}\big[\boldsymbol{e}_1\otimes\boldsymbol{e}_1 - \tfrac{1}{2}(\boldsymbol{e}_2\otimes\boldsymbol{e}_2+\boldsymbol{e}_3\otimes\boldsymbol{e}_3)\big] + \tfrac{1}{2}a^{3/2}\dot{\gamma}(\boldsymbol{e}_1\otimes\boldsymbol{e}_2+\boldsymbol{e}_2\otimes\boldsymbol{e}_1), \\ \boldsymbol{W} &= \tfrac{1}{2}a^{3/2}\dot{\gamma}(\boldsymbol{e}_1\otimes\boldsymbol{e}_2-\boldsymbol{e}_2\otimes\boldsymbol{e}_1). \end{aligned} \tag{104}$$

From these expressions is can be seen that a controls the rates of stretching of material fibers and γ controls shearing.

Two modes of simple deformation are considered:

(1) cyclic isochoric extension and contraction, and

(2) simple shear.

For cyclic isochoric extension and contraction, a and γ are specified by

$$a = 1 + 0.1\sin(2\pi t), \qquad \gamma = 0. \tag{105}$$

In particular, for this loading it can be shown that

$$\begin{gathered} \bar{\boldsymbol{B}}_\mathrm{e} = a_\mathrm{e}^2\boldsymbol{e}_1\otimes\boldsymbol{e}_1 + \frac{1}{a_\mathrm{e}}(\boldsymbol{e}_2\otimes\boldsymbol{e}_2+\boldsymbol{e}_3\otimes\boldsymbol{e}_3), \\ \boldsymbol{N}' = \sqrt{\tfrac{2}{3}}\big[\boldsymbol{e}_1\otimes\boldsymbol{e}_1 - \tfrac{1}{2}(\boldsymbol{e}_2\otimes\boldsymbol{e}_2+\boldsymbol{e}_3\otimes\boldsymbol{e}_3)\big], \\ \bar{\boldsymbol{B}}'_\mathrm{e} = B_\mathrm{e}\boldsymbol{N}', \quad B_\mathrm{e} = \sqrt{\tfrac{2}{3}}\Big(a_\mathrm{e}^2 - \frac{1}{a_\mathrm{e}}\Big), \\ U = \operatorname{sign}(B_e), \quad \boldsymbol{U} = U\boldsymbol{N}', \quad \boldsymbol{\beta} = \beta\boldsymbol{N}', \end{gathered} \tag{106}$$

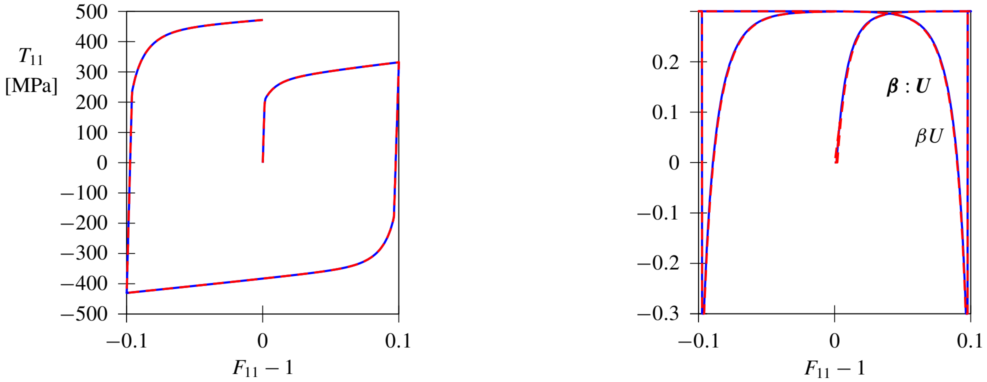

Figure 5. Isochoric extension and contraction: model T (solid blue lines) and S (dashed red lines). Left: stress-strain response. Right: evolution of βU and $\boldsymbol{\beta} : \boldsymbol{U}$ vs. strain.

where the function sign(x) is defined by

$$\operatorname{sign}(x) = \begin{cases} -1 & \text{for } x < 0, \\ 0 & \text{for } x = 0, \\ 1 & \text{for } x > 0. \end{cases} \tag{107}$$

Using these expressions with U and $\boldsymbol{U}$ being constants, it follows that the tensorial evolution equation (48) for $\boldsymbol{\beta}$ yields the same equation for β as the scalar equation (22). Also, the expressions (19) for the tensorial model and (25) for the scalar model yield the same value of H. Consequently, the two models yield exactly the same results for cyclic isochoric extension and contraction. This is illustrated in Figure 5. The tensorial model and the scalar-based model predict exactly the same stress-strain response in Figure 5, left, and also the same evolution for H in Figure 5, right. Even though it is not evident from Figure 5, right, it should be noted that the evolution of β vanishes during elastic deformation.

The main difference between the scalar model of directional hardening and the tensorial model can be seen for cyclic pure shear (TOR) for which U vanishes. For this loading, the scalar model exhibits no Bauschinger effect, whereas the tensorial model does. Although pure shear and simple shear are not identical, the following example considered cyclic simple shear specified by

$$a = 1, \quad \gamma = 0.1\sin(2\pi t), \tag{108}$$

to demonstrate the differences between the models.

Figure 6 shows the stress-strain response and the evolution of the relevant state variables for directional hardening for the two models. From Figure 6, left, it is evident that directional hardening is present in the tensorial model, whereas the scalar model only exhibits isotropic hardening for this load case. The reason is that for this load case, the loading variable U is close to zero, implying that directional hardening is not activated in the scalar model. This is further illustrated in Figure 6, right, where $\boldsymbol{\beta} : \boldsymbol{U}$ evolves whereas βU for the scalar model remains close to zero. There is, in fact, some evolution of β due to the fact that for large deformations and nonlinear kinematics, U is not exactly zero, but β remains very small in comparison to $\boldsymbol{\beta}$.

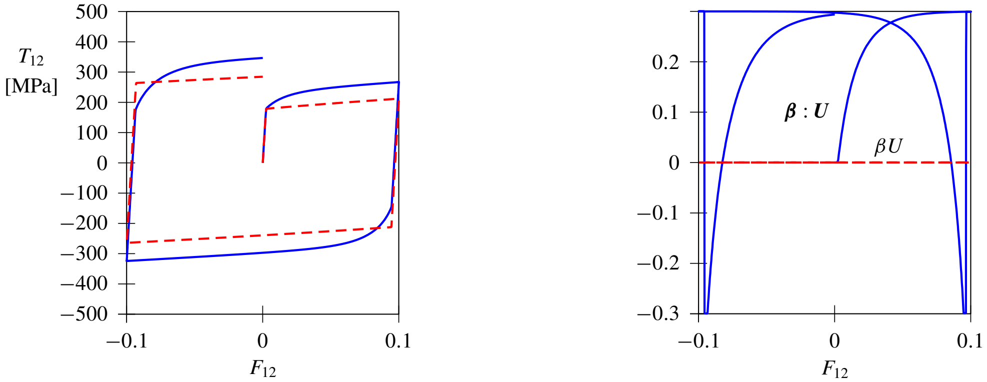

Figure 6. Cyclic loading in simple shear: model T (solid blue lines) and model S (dashed red lines). Left: stress-strain response. Right: evolution of βU and $\boldsymbol{\beta} : \boldsymbol{U}$ vs. strain.

6.4. ***Cyclic extension and contraction followed by simple shear.*** A load case is now considered where the material is first exposed to a cycle of isochoric extension and contraction, in accordance with the paths in Figure 5. After that, the material is exposed to a cycle of simple shear, as discussed in the previous subsection. In Figure 7, the stress-strain response and the evolution of the relevant directional hardening variable during the shearing cycle are shown.

During the preceding extension/contraction cycle the material has accumulated both isotropic and directional hardening. The evolution of the stress components T_{11}, T_{22}, and T_{33} is identical for models T and S, i.e., these components quickly drop to zero (or close to zero) once the extension/contraction loading mode ceases and the shearing mode is initiated. The shear stress curves in Figure 7, bottom-left, show a higher amplitude than the corresponding curves without any preceding deformation shown in Figure 6, left. In the tensorial model, directional hardening is accumulated in the variables β_{11}, β_{22}, and β_{33} during the first isochoric extension/contraction. Hence, when the shear loading starts, the evolution of β_{12} virtually starts from zero. This interaction causes an initial drop in $\boldsymbol{\beta}:\boldsymbol{U}$, as seen in Figure 7, bottom-right. However, when β_{12} has accumulated some hardening, $\boldsymbol{\beta}:\boldsymbol{U}$ soon starts to increase again. For the scalar-based model, directional hardening is accumulated in β during the isochoric extension/contraction cycle. During the shear loading, the hardening value decreases from 0.3 down to zero, since U is close to zero for this load case.

6.5. ***Cyclic loading with complex a deformation mode.*** A load case is now considered where the material is exposed to a more complex loading mode, i.e., a combination of isochoric extension and shearing. For this case, the velocity gradient is specified in the form

$$\begin{aligned} \boldsymbol{L} = \boldsymbol{D} = \boldsymbol{D}' &= D\sqrt{\tfrac{3}{2}}[\cos 2\pi t\, \boldsymbol{U}_{\mathrm{E}} + \sin 2\pi t\, \boldsymbol{U}_{\mathrm{S}}], \\ \boldsymbol{U}_{\mathrm{E}} &= \sqrt{\tfrac{2}{3}}\big[\boldsymbol{e}_1 \otimes \boldsymbol{e}_1 - \tfrac{1}{2}(\boldsymbol{e}_2 \otimes \boldsymbol{e}_2 + \boldsymbol{e}_3 \otimes \boldsymbol{e}_3)\big], \\ \boldsymbol{U}_{\mathrm{S}} &= \tfrac{1}{\sqrt{2}}[\boldsymbol{e}_1 \otimes \boldsymbol{e}_2 + \boldsymbol{e}_2 \otimes \boldsymbol{e}_1], \\ \boldsymbol{U}_{\mathrm{E}} : \boldsymbol{U}_{\mathrm{E}} = 1, &\quad \boldsymbol{U}_{\mathrm{S}} : \boldsymbol{U}_{\mathrm{S}} = 1, \quad \boldsymbol{U}_{\mathrm{E}} : \boldsymbol{U}_{\mathrm{S}} = 0, \end{aligned} \tag{109}$$

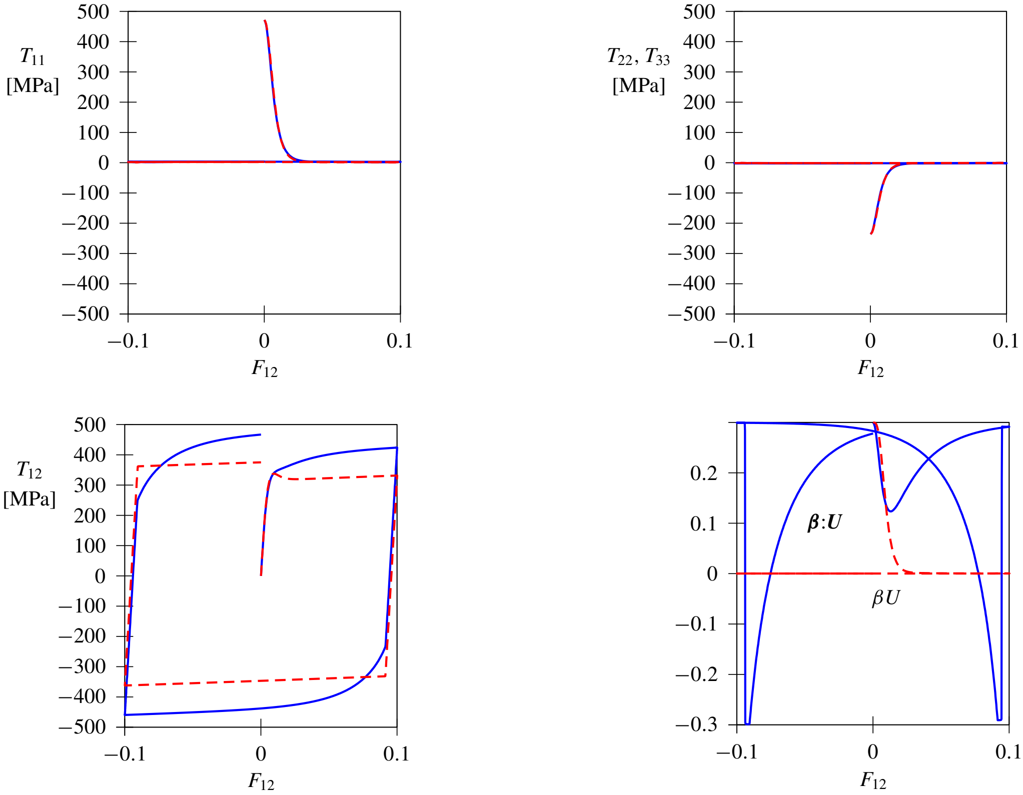

Figure 7. Cyclic loading in simple shear that was preceded by one cycle of isochoric extension and contraction: model T (solid blue lines) and model S (dashed red lines). Top and bottom-left: stress-strain response. Bottom-right: evolution of βU and $\boldsymbol{\beta} : \boldsymbol{U}$ vs. strain.

where $D = 1\text{s}^{-1}$. The deformation gradient is then attained by integrating the evolution equation

$$\dot{\boldsymbol{F}} = \boldsymbol{L}\boldsymbol{F}, \qquad \boldsymbol{F}(0) = \boldsymbol{I}. \tag{110}$$

In Figure 8, the outcome from the complex loading path is shown. The responses for T'_{11}, T'_{22}, and T'_{33} in Figure 8, top, for models T and S are virtually identical. The responses for T_{12} for models T and S differ somewhat. Especially the stress peaks differ by about 100 MPa between models T and S. The associated variations in βU and $\boldsymbol{\beta}{:}\boldsymbol{U}$ are shown in Figure 8, bottom-right. In the beginning of the load path, both $\boldsymbol{\beta}{:}\boldsymbol{U}$ and βU quickly approach the saturation level $\beta_{\text{s}} = 0.3$. The value of $\boldsymbol{\beta}{:}\boldsymbol{U}$ then decreases slowly during the rest of the loading cycle, whereas βU oscillates between β_{s} and (approximately) zero.

6.6. ***Cyclic loading of a plate with a circular hole.*** As a last numerical example, cyclic deformation of a plate with a circular hole is considered. In order to study this 3D problem, the material model was implemented in Abaqus as a UMAT user subroutine. The geometry of the plate is shown in Figure 9. The outer dimensions of the plate are given by $H_{\text{p}} = 4\text{cm}$ and $B_{\text{p}} = 2\text{cm}$. The radius of the central hole is $R_{\text{p}} = 1\text{cm}$, and the thickness of the plate is $T_{\text{p}} = 2\text{mm}$.

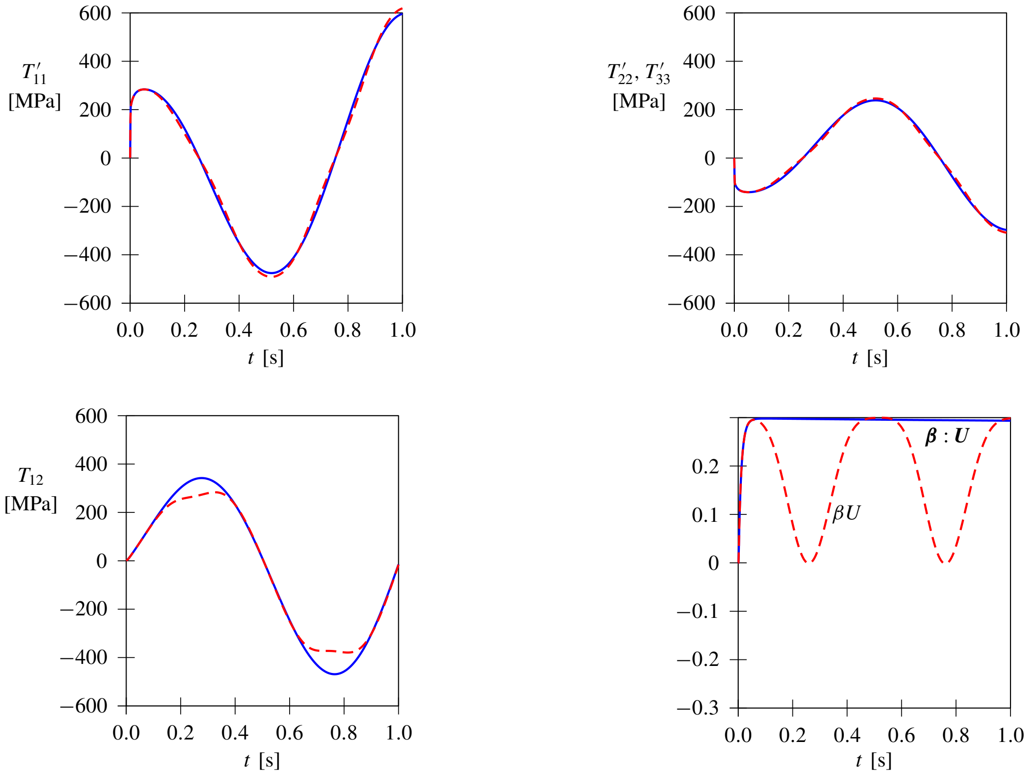

Figure 8. Cyclic loading in combined isochoric extension and contraction and simple shear: model T (solid blue lines) and model S (dashed red lines). Top and bottom-left: stress vs. time response. Bottom-right: evolution of βU and $\boldsymbol{\beta} : \boldsymbol{U}$ vs. time.

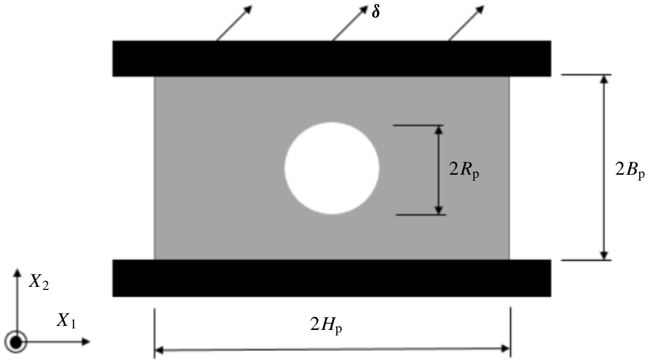

Figure 9. Geometry and loading of plate with a hole.

The plate (gray) is clamped between two rigid blocks (black). The lower block is fixed, whereas the upper block moves with a pure translation, $\boldsymbol{\delta}$, relative to the lower block. The translation is defined by

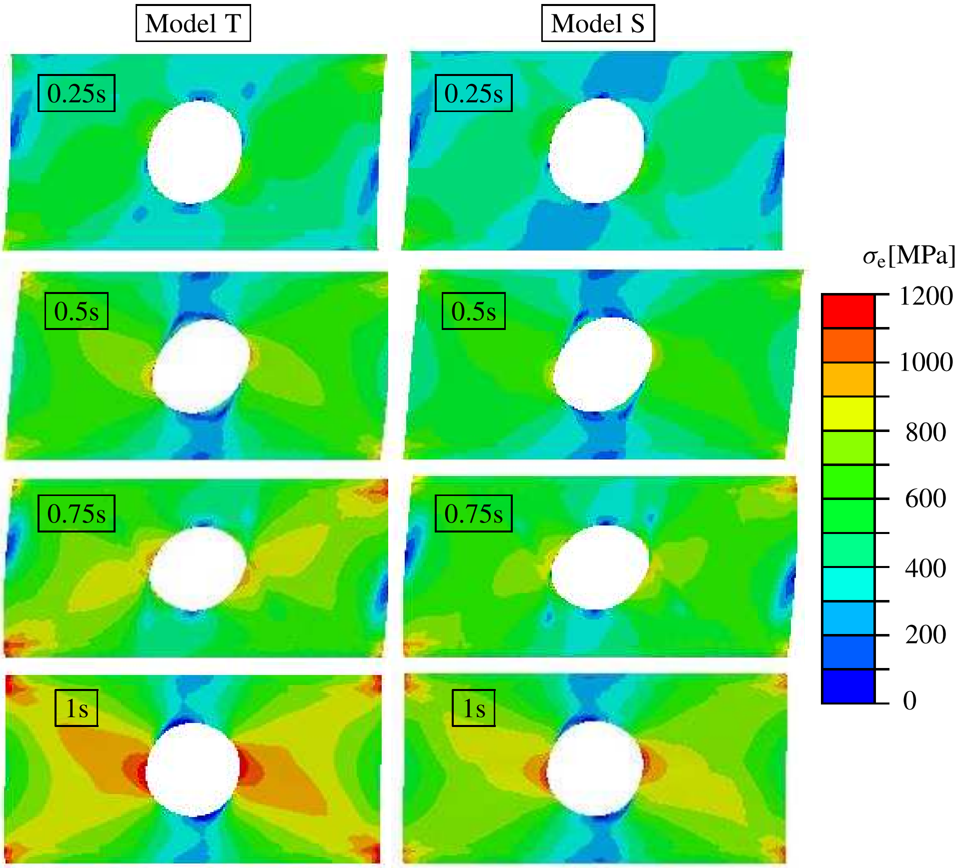

Figure 10. Distributions of σ_e at $t = 0.25$ s, 0.5 s, 0.75 s, and 1 s.

the velocities

$$\dot{\delta}_1 = 4\pi \cos(2\pi t)\,\text{mm/s}, \quad \dot{\delta}_2 = 4\pi \sin(2\pi t)\,\text{mm/s}, \quad t \in [0, 1], \tag{111}$$

implying that the upper block moves in a circle, causing a combination of tension/compression and shearing of the plate.

Wedge elements (i.e., triangular elements with thickness) with quadratic shape functions were used in the finite element analyses, and the characteristic length of the elements close to the hole, where the gradients of stress and strain are strongest, was 1 mm. One layer of elements was used in the thickness (X_3) direction of the plate. Due to symmetry, only half the plate was modeled in the through thickness direction, the material was allowed to slide freely on the symmetry plane $X_3 = 0$ and the surface of the plate was traction free.

Figures 10–13 show results from the plate simulations. In Figure 10, the distribution of the von Mises stress, σ_e, is shown at four different times. In general, the peaks in the stress fields are more pronounced in the solutions for model T than for model S. Besides that, the patterns of the stress fields are very similar for the two models. It can also be noted, that for this type of boundary condition, where the plate is fixed to the rigid blocks, significant stress concentrations appear at the corners of the plate. In the areas

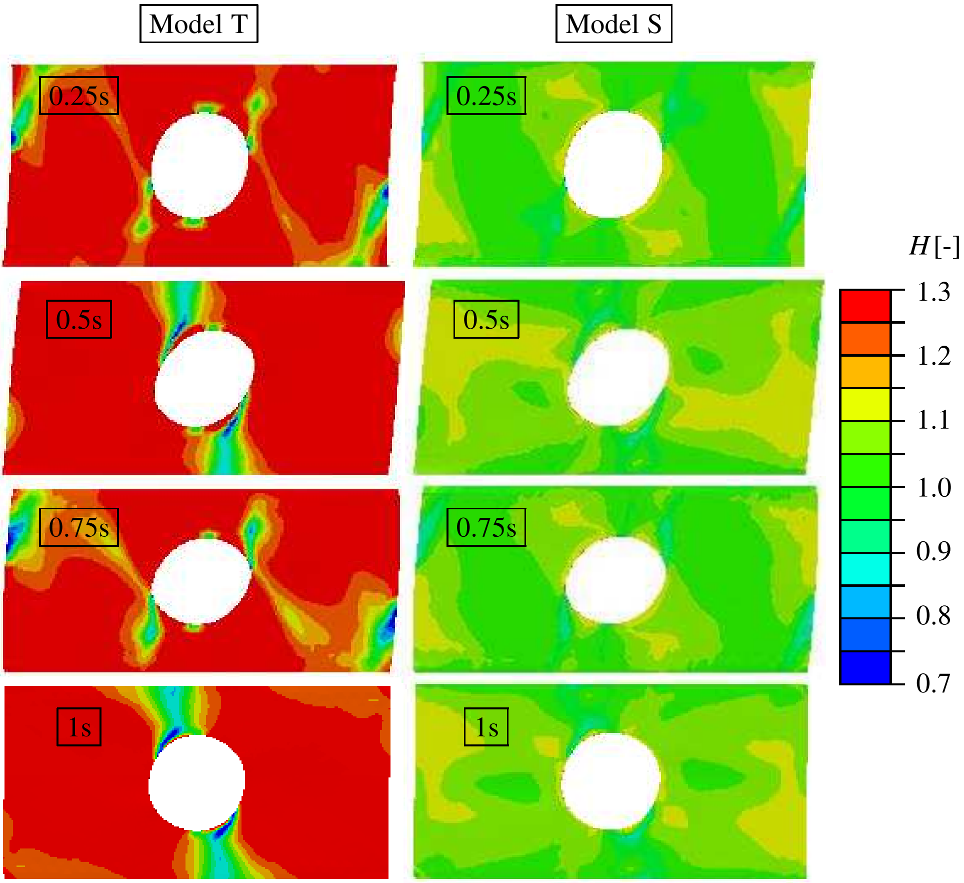

Figure 11. Distributions of (left) H_T and (right) H_S at $t = 0.25$ s, 0.5 s, 0.75 s, and 1 s.

at the hole where the highest stress peaks appear, the peak stress differs by about 100 MPa between the two models.

In Figure 11, distributions of the functions for directional hardening, i.e., H_T and H_S, are shown. The discrepancy between H_T and H_S is significant, where large areas of H_T are more or less saturated with $H_\mathrm{T} \approx 1 + \beta_\mathrm{s} = 1.3$, whereas the distribution of H_S doesn't deviate much from unity. This observation holds not only at the end of the simulation but also for the earlier stages of the simulation, as seen in the upper images in Figure 11.

Figure 12 shows the distribution of the effective hardening, i.e., κH, for the two models and at the same points in time as before. It can be seen, that the difference in total hardening is not as dramatic as the difference in the H-function. This is also the reason why, in the end, the distributions of effective stress for the two models in Figure 10 agree fairly well.

Finally, Figure 13 shows the distributions of the accumulated equivalent inelastic strain ε_p. By definition, this entity can only increase at a material point. The distribution of this entity is very similar for the two models, not only in the final state of the analysis, but throughout the analysis. Again, the corners of the plate experience stress concentrations with large cyclic shear stresses, which cause large amounts of

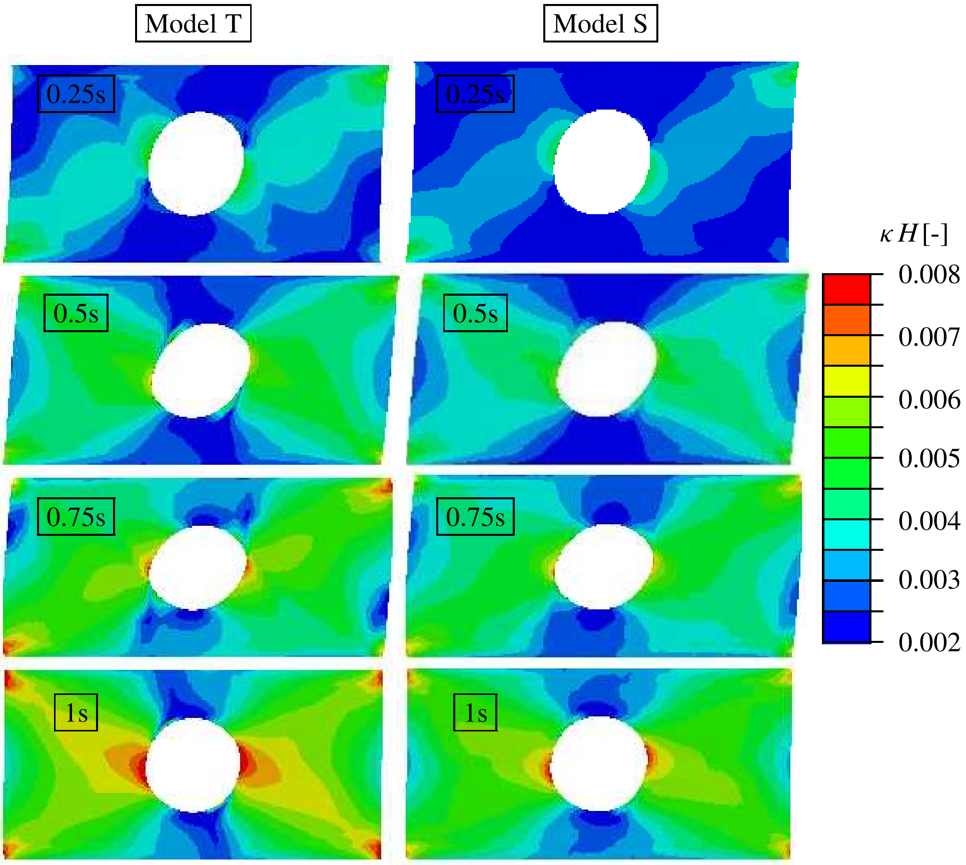

Figure 12. Distributions of (left) κH_{T} and (right) κH_{S} at $t = 0.25$ s, 0.5 s, 0.75 s, and 1 s.

accumulated inelastic strain. Peaks in the equivalent inelastic strain also appear to the left and right of the hole. The magnitude of these peaks is more or less the same for the two models.

7. Discussion and concluding remarks

One approach to modeling the Bauschinger effect is to introduce a history-dependent back-stress tensor with the stress in a yield function replaced by the difference of the stress and the back-stress. Directional hardening is an alternative approach which introduces a history-dependent directional hardening tensor $\boldsymbol{\beta}$ with the effective hardening being a function of isotropic hardening κ and the inner product of $\boldsymbol{\beta}$ with a normalized stress (or elastic deformation) tensor. The main idea of the present work is to propose a simplified version of directional hardening which introduces a history-dependent directional hardening scalar instead of a history-dependent directional hardening tensor. To test this idea, the predictions of scalar model are compared with those of the tensorial model.

Example problems indicate that the two models predict the same response for cyclic proportional triaxial extension and triaxial compression loadings. In contrast, for cyclic proportional pure torsion loading the tensorial model predicts a Bauschinger effect but the scalar model does not. However, in

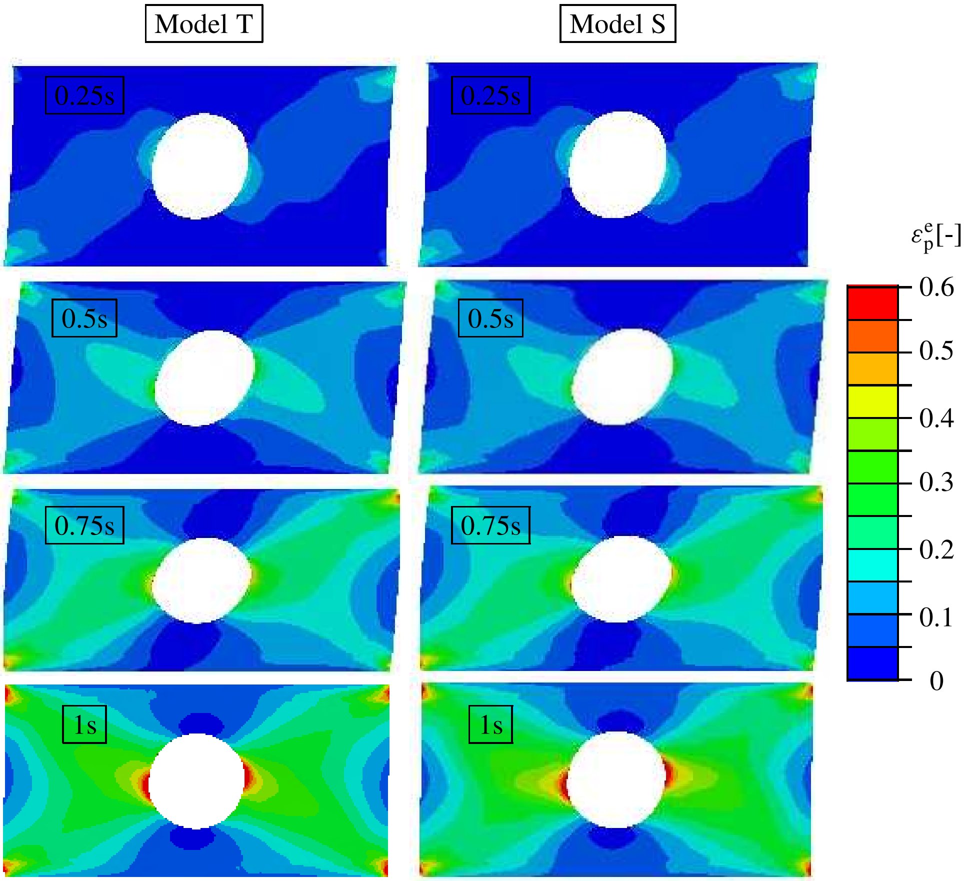

Figure 13. Distributions of equivalent plastic strain ε_p at $t = 0.25$ s, 0.5 s, 0.75 s, and 1 s.

practical problems the stress field is usually inhomogeneous so the material is not in a state of pure torsion. Consequently, additional examples with complex nonproportional loading paths were considered which indicate that the discrepancy between the two models in terms of stress levels is not dramatic. For the 3D analysis of a plate with a hole, the amplitudes of the peak stresses around the hole differed by less than 10% between the two models even though the value of $\beta_s = 0.3$ would indicate a potential effective yield stress κH in the range of $0.7\kappa \leq \kappa H \leq 1.3\kappa$.

Strongly objective numerical algorithms were developed to integrate the evolution equations for both models. Also, a consistent tangent operator was developed for both models. Obviously, the numerical implementation of the scalar model is significantly less complicated than for the tensorial model. Overall, the scalar model accounts for directional hardening fairly well and the simplicity of the model makes it an attractive option to add to isotropic hardening models.

Acknowledgements

The authors would like to thank Prof. P. Steinmann for helpful comments.

References

[Armstrong and Frederick 1966] P. J. Armstrong and C. O. Frederick, "A mathematical representation of the multiaxial Bauschinger effect", technical report 731, Central Elect. Generating Board, 1966. Reprinted with supplemental material in *Mater. High Temp.* **24**:1 (2007), 1–26.

[Bammann 1990] D. J. Bammann, "Modeling temperature and strain rate dependent large deformations of metals", *Appl. Mech. Rev.* (*ASME*) **43**:5S (1990), S312–S319.

[Barlat et al. 2011] F. Barlat, J. J. Gracio, M.-G. Lee, E. F. Rauch, and G. Vincze, "An alternative to kinematic hardening in classical plasticity", *Int. J. Plast.* **27**:9 (2011), 1309–1327.

[Bauschinger 1881] J. Bauschinger, "Über die Veränderung der Elasticitätgenze und des Elasticitätmodulus verschiedener Metalle", *Civilingenjeur* **27** (1881), 289–348.

[Besseling 1958] J. R. Besseling, "A theory of elastic, plastic and creep deformations of an initially isotropic material showing anisotropic strain-hardening, creep recovery, and secondary creep", *J. Appl. Mech.* **25** (1958), 529–536.

[Bodner 1968] S. R. Bodner, "Constitutive equations for dynamic material behavior", pp. 176–190 in *Mechanical behaviour of materials under dynamic loads*, edited by U. S. Lindholm, Springer, 1968.

[Chaboche 2008] J. L. Chaboche, "A review of some plasticity and viscoplasticity constitutive theories", *Int. J. Plast.* **24**:10 (2008), 1642–1693.

[Chan et al. 1988] K. S. Chan, S. R. Bodner, and U. S. Lindholm, "Phenomenological modeling of hardening and thermal recovery in metals", *J. Eng. Mater. Technol.* (*ASME*) **110**:1 (1988), 1–8.

[Choteau et al. 2005] M. Choteau, P. Quaegebeur, and S. Degallaix, "Modelling of Bauschinger effect by various constitutive relations derived from thermodynamical formulation", *Mech. Mater.* **37**:11 (2005), 1143–1152.

[Eckart 1948] C. Eckart, "The thermodynamics of irreversible processes, IV: The theory of elasticity and anelasticity", *Phys. Rev.* **73**:4 (1948), 373–382.

[Gladman 2018] B. Gladman, "LS-DYNA keyword user's manual, II: Material models", software manual, 2018, Available at https://tinyurl.com/lsdynar902. Version R11.

[Hollenstein et al. 2013] M. Hollenstein, M. Jabareen, and M. B. Rubin, "Modeling a smooth elastic-inelastic transition with a strongly objective numerical integrator needing no iteration", *Comput. Mech.* **52**:3 (2013), 649–667. Corrected in **55**:2 (2015), 453.

[Langer et al. 2010] J. S. Langer, E. Bouchbinder, and T. Lookman, "Thermodynamic theory of dislocation-mediated plasticity", *Acta Mater.* **58**:10 (2010), 3718–3732.

[Le and Tran 2018] K. C. Le and T. M. Tran, "Thermodynamic dislocation theory: Bauschinger effect", *Phys. Rev. E* **97**:4 (2018), art. id. 043002.

[Leonov 1976] A. I. Leonov, "Nonequilibrium thermodynamics and rheology of viscoelastic polymer media", *Rheol. Acta* **15** (1976), 85–98.

[Papes 2012] O. Papes, *Nonlinear continuum mechanics in modern engineering applications*, Ph.D. thesis, ETH Zürich, 2012, Available at https://doi.org/10.3929/ethz-a-007139775.

[Prager 1949] W. Prager, "Recent developments in the mathematical theory of plasticity", *J. Appl. Phys.* **20** (1949), 235–241.

[Rubin 1991] M. B. Rubin, "Simple, convenient isotropic failure surface", *J. Eng. Mech.* (*ASCE*) **117**:2 (1991), 348–369.

[Rubin 2012] M. B. Rubin, "Removal of unphysical arbitrariness in constitutive equations for elastically anisotropic nonlinear elastic-viscoplastic solids", *Int. J. Eng. Sci.* **53** (2012), 38–45.

[Rubin 2020] M. B. Rubin, "A strongly objective expression for the average deformation rate with application to numerical integration algorithms", *Finite Elem. Anal. Des.* **175** (2020), art. id. 103409.

[Rubin and Attia 1996] M. B. Rubin and A. Attia, "Calculation of hyperelastic response of finitely deformed elastic-viscoplastic materials", *Int. J. Numer. Methods Eng.* **39**:2 (1996), 309–320.

[Rubin and Bodner 1995] M. B. Rubin and S. R. Bodner, "An incremental elastic-viscoplastic theory indicating a reduced modulus for non-proportional buckling", *Int. J. Solids Struct.* **32**:20 (1995), 2967–2987.

[Rubin and Cardiff 2017] M. B. Rubin and P. Cardiff, "Advantages of formulating an evolution equation directly for elastic distortional deformation in finite deformation plasticity", *Comput. Mech.* **60**:5 (2017), 703–707.

[Rubin and Papes 2011] M. B. Rubin and O. Papes, "Advantages of formulating evolution equations for elastic-viscoplastic materials in terms of the velocity gradient instead of the spin tensor", *J. Mech. Mater. Struct.* **6**:1-4 (2011), 529–543.

[Ruess 1935] E. Ruess, "Abstract", pp. 91 in *Proc. Fourth Int. Cong. Appl. Mech.* (Cambridge, England, 1934), Cambridge University Press, 1935.

[Simo 1988] J. C. Simo, "A framework for finite strain elastoplasticity based on maximum plastic dissipation and the multiplicative decomposition, II: Computational aspects", *Comput. Methods Appl. Mech. Eng.* **68**:1 (1988), 1–31.

[Simo 1992] J. C. Simo, "Algorithms for static and dynamic multiplicative plasticity that preserve the classical return mapping schemes of the infinitesimal theory", *Comput. Methods Appl. Mech. Eng.* **99**:1 (1992), 61–112.

[Simo 1998] J. C. Simo, "Numerical analysis and simulation of plasticity", pp. 183–499 in *Handbook of numerical analysis, VI*, edited by P. G. Ciarlet and J. L. Lions, North-Holland, Amsterdam, 1998.

[Simo and Hughes 1998] J. C. Simo and T. J. R. Hughes, *Computational inelasticity*, Interdisc. Appl. Math. **7**, Springer, 1998.

[Sowerby et al. 1979] R. Sowerby, D. K. Uko, and Y. Tomita, "A review of certain aspects of the Bauschinger effect in metals", *Mater. Sci. Eng.* **41**:1 (1979), 43–58.

[Wilkins 1963] M. L. Wilkins, "Calculation of elastic-plastic flow", technical report 7322, Lawrence Radiation Lab., 1963, Available at https://tinyurl.com/radiatlab.

Received 9 Mar 2020. Revised 1 Jun 2020. Accepted 7 Jun 2020.

MARTIN KROON: `martin.kroon@lnu.se`
Department of Mechanical Engineering, Linnaeus University, Växjö, Sweden

M. B. RUBIN: `mbrubin@tx.technion.ac.il`
Faculty of Mechanical Engineering, Technion - Israel Institute of Technology, Haifa, Israel

JOURNAL OF MECHANICS OF MATERIALS AND STRUCTURES

msp.org/jomms

Founded by Charles R. Steele and Marie-Louise Steele

EDITORIAL BOARD

Adair R. Aguiar	University of São Paulo at São Carlos, Brazil
Katia Bertoldi	Harvard University, USA
Davide Bigoni	University of Trento, Italy
Maenghyo Cho	Seoul National University, Korea
Huiling Duan	Beijing University
Yibin Fu	Keele University, UK
Iwona Jasiuk	University of Illinois at Urbana-Champaign, USA
Dennis Kochmann	ETH Zurich
Mitsutoshi Kuroda	Yamagata University, Japan
Chee W. Lim	City University of Hong Kong
Zishun Liu	Xi'an Jiaotong University, China
Thomas J. Pence	Michigan State University, USA
Gianni Royer-Carfagni	Università degli studi di Parma, Italy
David Steigmann	University of California at Berkeley, USA
Paul Steinmann	Friedrich-Alexander-Universität Erlangen-Nürnberg, Germany
Kenjiro Terada	Tohoku University, Japan

ADVISORY BOARD

J. P. Carter	University of Sydney, Australia
D. H. Hodges	Georgia Institute of Technology, USA
J. Hutchinson	Harvard University, USA
D. Pamplona	Universidade Católica do Rio de Janeiro, Brazil
M. B. Rubin	Technion, Haifa, Israel

PRODUCTION production@msp.org

Silvio Levy Scientific Editor

Cover photo: Mando Gomez, www.mandolux.com

See msp.org/jomms for submission guidelines.

JoMMS (ISSN 1559-3959) at Mathematical Sciences Publishers, 798 Evans Hall #6840, c/o University of California, Berkeley, CA 94720-3840, is published in 10 issues a year. The subscription price for 2020 is US $660/year for the electronic version, and $830/year (+$60, if shipping outside the US) for print and electronic. Subscriptions, requests for back issues, and changes of address should be sent to MSP.

JoMMS peer-review and production is managed by EditFlow® from Mathematical Sciences Publishers.

PUBLISHED BY
mathematical sciences publishers
nonprofit scientific publishing
http://msp.org/

© 2020 Mathematical Sciences Publishers

Journal of Mechanics of Materials and Structures

Volume 15, No. 4 July 2020

Wave propagation in three-dimensional graphene aerogel cylindrical shells resting on Winkler–Pasternak elastic foundation
CHEN LIANG and YAN QING WANG 435

Semiinfinite moving crack in a shear-free orthotropic strip
SANATAN JANA, PRASANTA BASAK and SUBHAS MANDAL 457

A Bernoulli–Euler beam model based on the local gradient theory of elasticity
OLHA HRYTSYNA 471

Nonlinear deflection experiments: wrinkling of plates pressed onto foundations
NICHOLAS J. SALAMON and PEGGY B. SALAMON 489

Buckling of circular CFDST slender columns with compliant interfaces: exact solution
SIMON SCHNABL and BOJAN ČAS 499

A simple scalar directional hardening model for the Bauschinger effect compared with a tensorial model
MARTIN KROON and M. B. RUBIN 511

Closed-form solutions for an edge dislocation interacting with a parabolic or elliptical elastic inhomogeneity having the same shear modulus as the matrix
XU WANG and PETER SCHIAVONE 539